

Materials Science and Engineering: Concepts, Methodologies, Tools, and Applications

Information Resources Management Association
USA

Volume II



www.igi-global.com

Published in the United States of America by

IGI Global
Engineering Science Reference (an imprint of IGI Global)
701 E. Chocolate Avenue
Hershey PA, USA 17033
Tel: 717-533-8845
Fax: 717-533-8661
E-mail: cust@igi-global.com
Web site: <http://www.igi-global.com>

Copyright © 2017 by IGI Global. All rights reserved. No part of this publication may be reproduced, stored or distributed in any form or by any means, electronic or mechanical, including photocopying, without written permission from the publisher. Product or company names used in this set are for identification purposes only. Inclusion of the names of the products or companies does not indicate a claim of ownership by IGI Global of the trademark or registered trademark.

Library of Congress Cataloging-in-Publication Data

Names: Information Resources Management Association editor.

Title: Materials science and engineering : concepts, methodologies, tools,
and applications / Information Resources Management Association, editor.

Other titles: Materials science and engineering (Hershey, Pa.)

Description: Hershey, PA : Engineering Science Reference, [2017]

Identifiers: LCCN 2016046226 | ISBN 9781522517986 (hardcover) | ISBN
9781522517993 (ebook)

Subjects: LCSH: Materials.

Classification: LCC TA403 .M3467 2017 | DDC 620.1/1--dc23 LC record available at <https://lcn.loc.gov/2016046226>

British Cataloguing in Publication Data

A Cataloguing in Publication record for this book is available from the British Library.

All work contributed to this book is new, previously-unpublished material. The views expressed in this book are those of the authors, but not necessarily of the publisher.

For electronic access to this publication, please contact: eresources@igi-global.com.

Chapter 43

Practical Applications of X-Ray Line Profile Analysis

Jenő Gubicza

Eötvös Loránd University, Hungary

ABSTRACT

In the previous chapters, the theory and the main methods of diffraction peak profile analysis were presented. Additionally, the specialties in the measurement and the evaluation of line profiles in the cases of thin films and single crystals were discussed. In this chapter, some practical considerations are given in order to facilitate the evaluation of peak profiles and the interpretation of the results obtained by this method. For instance, the procedures for instrumental correction are overviewed. Additionally, how the prevailing dislocation slip systems and twin boundary types in hexagonal polycrystals can be determined from line profiles is shown. Besides the dislocation density, the vacancy concentration can also be obtained by the combination of electrical resistivity, calorimetric, and line profile measurements. The crystallite size and the twin boundary frequency determined by X-ray peak profile analysis are compared with the values obtained by the direct method of transmission electron microscopy. Furthermore, the limits of line profile analysis in the determination of crystallite size and defect densities are given. Finally, short overviews on the results obtained by peak profile analysis for metals, ceramics, and polymers are presented.

INTRODUCTION

The experimental settings of the X-ray diffractometer used in the measurement of line profiles and the preparation of the data before evaluation (e.g. background subtraction or truncation of peak angular range) influence the results obtained in peak profile analysis (Langford, 1968). For instance, the peak broadening increases with increasing the width of divergence and receiving slits used in the diffraction instrument (Wilson, 1963; Cheary & Cline, 1994). The contribution of instrumental effects to line broadening should be removed from the measured data in order to obtain the peak profiles caused purely by the microstructure. Both a wrong instrumental correction and a subsequent incorrect evaluation of diffraction peaks may result in systematic errors in the obtained parameters of the microstructure. For instance, when the range of the scattering angle, 2θ , for reflection 111 of cold-worked Ni was smaller

DOI: 10.4018/978-1-5225-1798-6.ch043

than five times the full width at half maximum (FWHM), the mean crystallite size determined from the Fourier transform was significantly smaller than the true value (Langford, 1968). The wrong background subtraction also alters the breadth and shape of peaks used in the evaluation procedures and therefore yields deviation from the true values of the crystallite size or the defect densities. Thus, besides the theory of X-ray line profile analysis some practical skills should also be known in order to obtain reliable results in peak profile analysis.

X-ray line profile analysis is an indirect method for the determination of the microstructure, therefore the evaluation of peak profiles and the interpretation of the results should be performed carefully. Usually, a reliable model of the microstructure is necessary for a correct evaluation of the profile shape (Ungár, Gubicza, Ribárik, & Borbély, 2001), which can be constructed with the help of complementary methods, such as transmission electron microscopy (TEM). However, the parameters of the microstructure determined from line profiles often differ from those obtained by other methods (e.g. by TEM), as the various experimental procedures study the microstructure from different aspects (Gubicza & Ungár, 2007; Samadi Khoshkhoo, Scudino, Thomas, Gemming, Wendrock, & Eckert, 2013). Thus, the viewpoint of line profile analysis in investigation of microstructure and the limits of this method in practice should be known. In this chapter useful practical considerations are presented in order to facilitate the evaluation of peak profiles and the interpretation of the obtained results. The microstructure parameters determined by line profile analysis are compared to the values obtained by microscopic methods.

INSTRUMENTAL CORRECTION

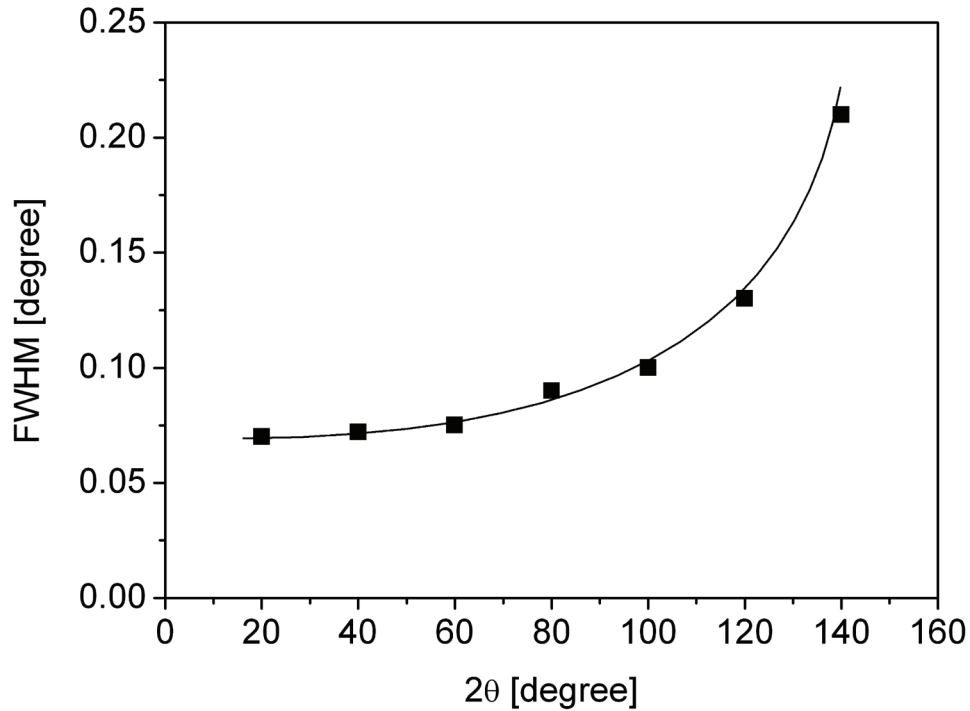
According to the kinematical scattering theory, for an infinite single crystal without any lattice distortions the Bragg peaks are Dirac-delta functions with infinitesimal breadth. The peak broadening decreases with increasing the size of crystallites and decreasing the lattice defect densities, but even for a very large perfect crystal the line breadth goes to a finite value which is referred to as Darwin width (Warren, 1990). In the practice, the peak broadening for a large perfect crystal can be further increased by instrumental effects. The most important factors influencing the shape and breadth of the instrumental peak profiles are (i) the size of X-ray source, (ii) the equatorial and axial divergences of the beam (observed parallel and perpendicular, respectively, to the plane of the incident and diffracted beams), (iii) the width of the receiving slit, (iv) the specimen transparency, (v) the distribution of wavelength of the incident beam (spectral dispersion) and (vi) the misalignment of the diffractometer (Cernansky, 2000). The line breadth caused by the instrumental effects is referred to as “instrumental broadening” which should be taken into account in the evaluation of peak profiles. The total instrumental profile is a convolution of the peaks caused by the different instrumental effects listed above. The instrumental peak profiles for a given diffraction setting can be measured on a standard material which has large crystals with small amount of lattice imperfections. Then, these instrumental profiles can be used for instrumental correction in further experiments carried out under the same instrumental conditions. For the determination of the instrumental broadening the most often used material is the LaB_6 standard (Langford & Louer, 1996). Other materials are also used as instrumental standards, such as annealed BaF_2 (Louer & Langford, 1988) and KCl (Scardi, Lutterotti, & Maistrelli, 1994). Besides the large crystallite size and the very small lattice distortions there is an extra advantage of the application of LaB_6 as a line profile standard material, namely it has many peaks distributed more or less equidistantly in the diffraction pattern. The large number of peaks for the standard material is beneficial since the instrumental broadening varies

with the scattering angle, therefore the closest instrumental peak should be used for the correction of a measured profile. The specimen transparency yields an asymmetric angle-dependent component into the instrumental broadening. In order to reduce the effect of transparency on the instrumental profile, the standard material should have a high linear absorption coefficient (e.g. LaB_6 and BaF_2), unless a very thin sample are used for instrumental correction. Generally, the line profile standard material should have similar transparency as for the studied sample. Therefore, although KCl as a standard material may introduce a measurable breadth contribution due to its high transparency, it can be used for correcting profiles obtained on materials with a similar absorption coefficient (e.g. for many ceramics). Applying parallel-beam optics (i.e. when the transparency effect is marginal) the instrumental breadth measured on KCl was lower than that obtained for either BaF_2 or LaB_6 , although the difference between KCl and LaB_6 was very small (Scardi, Leoni, & Langford, 1998).

The variation of the FWHM of the instrumental line profiles with the scattering angle, 2θ , is illustrated in Figure 1 for a conventional Bragg–Brentano diffractometer with an incident-beam monochromator and a 0.05° receiving slit (Louer & Langford, 1988). It can be seen that at low angles the instrumental line broadening is about 0.07° , and above $2\theta=80^\circ$ it increases rapidly with increasing scattering angle. For a synchrotron X-ray source with a 0.026° receiving slit the instrumental breadth is half as large as the values plotted in Figure 1. Generally, the application of parallel-beam optics instead of parafocusing Bragg-Brentano geometry with divergent beam reduces the aberrations caused by the specimen surface displacement and the sample transparency (Scardi, Leoni, & Langford, 1998). Additionally, the application of a Soller-slit assembly instead of a conventional receiving slit in parallel beam optics yields a reduction of the instrumental broadening (Scardi, Leoni, Cappuccio, Langford, & Cernik, 1996). The instrumental breadth at synchrotron radiation source equipped with Soller-slit increases from 0.04° to 0.08° when the diffraction angle increased from $\sim 20^\circ$ to $\sim 120^\circ$ wavelength of 0.154 nm. The instrumental profiles fitted by pseudo-Voigt functions are more Gaussian in character which is reduced with increasing the scattering angle and the peaks become more Lorentzian. The change of the shape of the instrumental profiles with increasing the scattering angle can be attributed to the variation of the contributions of the different instrumental factors. At low angles the instrumental broadening is determined mainly by the size of the receiving slit, while at high angles the influence of wavelength dispersion in the incident beam is the dominant factor (Scardi, Leoni, & Langford, 1998). The disadvantage of a Soller-slit assembly is that two weak satellite peaks appear at both sides of the fundamental reflections of the standard material (at about 0.2° from the center of the main peak). These satellite peaks are due to the slight non-parallelism of the foils in the Soller-slit assembly (Scardi, Leoni, Cappuccio, Langford, & Cernik, 1996). The intensity of the satellites is a few percent of that of the main peak. If Debye-Scherrer diffraction geometry is used with capillary sample holder, the capillary displacement and diameter also result in considerable contributions to instrumental broadening (Gozzo, Cervellino, Leoni, Scardi, Bergamaschi, & Schmitt, 2010). It is noted that besides the measurement of the instrumental pattern on standard materials, the instrumental peaks can also be determined by first principle calculations from the instrument geometry and the spectral dispersion of X-ray radiation (Cheary & Coelho, 1992; Zuev, 2006). A detailed analysis on the instrumental effects related to polycapillary optics has been presented by Leoni, Welzel, and Scardi (2004). In the following, the basic procedures for instrumental correction are overviewed.

The experimental line profile (I_{exp}) is the convolution of the profile functions corresponding to the physical (caused by the microstructure) and the instrumental broadening contributions denoted by I_{phys} and I_{instr} , respectively (Warren, 1990):

Figure 1. The variation of the FWHM of the instrumental line profiles with the scattering angle 2θ for a conventional Bragg–Brentano diffractometer with an incident-beam monochromator and a 0.05° receiving slit (Louer & Langford, 1988)



$$I_{\text{exp}}(\kappa) = I_{\text{instr}}(\kappa) * I_{\text{phys}}(\kappa) = \int_{-\infty}^{\infty} I_{\text{instr}}(x) I_{\text{phys}}(\kappa - x) dx, \quad (9.1)$$

where the symbol “*” denotes the operation of convolution. The length of the scattering vector is given as

$$\kappa = \frac{2 \sin \theta}{\lambda},$$

where θ and λ are the half of the scattering angle and the wavelength of X-rays, respectively. As the physical and the instrumental profiles are in convolution, it is difficult to gain the physical profile directly from the measured diffraction peak. Stokes (1948) proposed a procedure for instrumental correction using the Fourier transforms of the profile components. The Fourier transform of a line profile can be calculated e.g. by discrete Fourier transformation (Klug & Alexander, 1974). Due to the properties of the Fourier transformation, the Fourier transform of the experimental profile (A_{exp}) is the product of the Fourier transforms of the physical and the instrumental profiles denoted by A_{phys} and A_{instr} , respectively. Therefore, to obtain the physical diffraction profile, first the Fourier transforms of the experimental and instrumental profiles should be calculated and then the former one should be divided by the latter one as:

$$A_{phys}(L) = \frac{A_{exp}(L)}{A_{instr}(L)}, \quad (9.2)$$

where L is the Fourier variable. This procedure referred to as Stokes-method results in the Fourier transform of the physical profile which should be inverse Fourier transformed in order to gain the physical intensity profile. It is noted that for an asymmetric profile, the Fourier transform has real and imaginary parts and in this case the division of the Fourier transforms should be made as for the complex numbers. The uncertainty of this calculation is relatively high for large values of the Fourier variable where nearly zero values of the Fourier transforms are divided by each other or when the instrumental broadening is very close to the experimental one. In the latter case instead of the Fourier transformation it is strongly recommended to calculate the convolution of the instrumental and the assumed physical profiles, and fit the function resulted by the convolution to the experimental profile by a computer program (e.g. in WPPM or CMWP methods, see chapter 6).

In practice, the Stokes correction procedure seems to be complicated, if X-ray radiation contains two wavelength components (e.g. $\text{CuK}\alpha_1$ and $\text{CuK}\alpha_2$). In this case the measured intensity profile is the sum of two curves with the same breadth and shape, but the intensity of component α_2 is half of that for component α_1 and its center appears at higher 2θ value due to the larger wavelength. The difference between the scattering angles of the centers of profiles α_1 and α_2 equals

$$\Delta(2\theta) = 2 \tan \theta \frac{\Delta\lambda}{\lambda},$$

where $\Delta\lambda$ is the wavelength difference. If the Bragg-angles of the experimental and the instrumental peaks are exactly the same, component α_2 disappears by the Stokes method, i.e. the result of the instrumental correction is the same as for single α_1 radiation. This is due to the linearity of the Fourier transformation and the same ratio of the intensities of components α_1 and α_2 for both experimental and instrumental reflections. In order to prove the above statement, the Fourier transform of the experimental peak should be expressed as:

$$\begin{aligned} A_{exp}(L) &= \int_{-\infty}^{\infty} I_{exp}^{\alpha_1}(\kappa) \exp(2\pi i \kappa L) dL + \int_{-\infty}^{\infty} I_{exp}^{\alpha_2}(\kappa) \exp(2\pi i \kappa L) dL = \\ &= \int_{-\infty}^{\infty} I_{exp}^{\alpha_1}(\kappa) \exp(2\pi i \kappa L) dL + \int_{-\infty}^{\infty} \frac{1}{2} I_{exp}^{\alpha_1}(\kappa - \kappa_0) \exp[2\pi i (\kappa - \kappa_0) L] \exp(2\pi i \Delta\kappa L) dL = \\ &= \frac{3}{2} A_{exp}^{\alpha_1}(L) \exp(2\pi i \Delta\kappa L) \end{aligned} \quad (9.3)$$

where $I_{exp}^{\alpha_1}$ and $I_{exp}^{\alpha_2}$ are the experimental intensity profiles corresponding to components α_1 and α_2 , respectively, $A_{exp}^{\alpha_1}$ is the Fourier transform of

$$I_{exp}^{\alpha_1} \text{ and } \Delta\kappa = \kappa \frac{\Delta\lambda}{\lambda}$$

Practical Applications of X-Ray Line Profile Analysis

is the difference between κ values corresponding to the centers of the two peak components. If the Bragg-angle of the instrumental peak is the same as for the experimental peak, then the corresponding values of $\Delta\kappa$ are also the same and the ratio of the Fourier transforms yields:

$$\frac{A_{\text{exp}}(L)}{A_{\text{instr}}(L)} = \frac{\frac{3}{2}A_{\text{exp}}^{\alpha_1}(L)\exp(2\pi i\Delta\kappa L)}{\frac{3}{2}A_{\text{instr}}^{\alpha_1}(L)\exp(2\pi i\Delta\kappa L)} = \frac{A_{\text{exp}}^{\alpha_1}(L)}{A_{\text{instr}}^{\alpha_1}(L)} = A_{\text{phys}}(L). \quad (9.4)$$

where $A_{\text{instr}}^{\alpha_1}$ is the Fourier transform of component α_1 in the instrumental profile. However, usually there is no instrumental peak at the exact Bragg-angle of the experimental profile, therefore the nearest instrumental peak is used in the Stokes correction. In this case, $A_{\text{exp}}^{\alpha_1}$ and $A_{\text{instr}}^{\alpha_1}$ can be calculated from A_{exp} and A_{instr} , respectively, using Equation (9.3). Then, the ratio of $A_{\text{exp}}^{\alpha_1}$ and $A_{\text{instr}}^{\alpha_1}$ yields A_{phys} . It is also possible that before the instrumental correction procedure component α_2 in the experimental profile is eliminated. A simple method for the separation of peak α_2 was introduced by Rachinger (1948). In the Rachinger correction procedure, starting from the small-angle side of the experimental peak where the intensity is considered to be zero, the abscissa of the profile function is divided into small intervals with the width of $\Delta(2\theta)/m$, where m is an integer. The intensity corresponds to peak component α_1 at the end of the i^{th} interval, $I_{\text{exp}}^{\alpha_1}(i)$, can be expressed by the intensity of the whole profile at the end of the i^{th} interval, $I_{\text{exp}}(i)$, and by the intensity of peak α_1 at the end of the $(i-m)^{\text{th}}$ interval:

$$I_{\text{exp}}^{\alpha_1}(i) = I_{\text{exp}}(i) - I_{\text{exp}}^{\alpha_2}(i) = I_{\text{exp}}(i) - \frac{1}{2}I_{\text{exp}}^{\alpha_1}(i-m). \quad (9.5)$$

Beginning at the small-angle side of the measured profile, the values of $I_{\text{exp}}^{\alpha_1}(i)$ can be obtained gradually using Equation (9.5). At the high angle side of the curve, this evaluation gives low accuracy of $I_{\text{exp}}^{\alpha_1}(i)$ since the subtraction of nearly equal quantities should be made. After the separation of peak components α_1 and α_2 , the Stokes correction can be carried out on $I_{\text{exp}}^{\alpha_1}$ using the similarly separated $I_{\text{instr}}^{\alpha_1}$.

As the experimental line profile is the convolution of the functions corresponding to the physical and the instrumental profiles, the relation between the breadths of the experimental, the physical and the instrumental peaks depends on their shapes. For instance, assuming Lorentzian-Lorentzian, Gaussian-Gaussian or Lorentzian-Gaussian line shapes for the physical-instrumental peak profile pairs, the various relationships between the integral breadths are presented in Equations (6.23)-(6.25) of chapter 6. It should be noted that both the breadth and shape of instrumental line profiles vary continuously with κ and tend to be approximately Gaussian at low diffraction angles and become progressively more Lorentzian at high values of 2θ due to the increase of wavelength dispersion (Louer & Langford, 1988; Langford, Cernik, & Louer, 1991). Since the diffraction peak profiles are not exact Lorentzian or Gaussian functions, the application of any relationship for instrumental correction of peak breadth is very uncertain.

DETERMINATION OF BURGERS-VECTOR POPULATION IN HEXAGONAL MATERIALS

In hexagonal materials there are eleven dislocation slip systems which are shown in Figure 11 in Chapter 3 and their Burgers vectors and slip planes are listed in Table 2 of Chapter 3. The effect of a dislocation type on the broadening of X-ray peak with the indices hkl is taken into account with the dislocation contrast factor C_{hkl} (see chapter 3). For hexagonal polycrystalline materials the average contrast factors \bar{C}_{hkl} can be written in the following form (Dragomir & Ungár, 2002):

$$\bar{C}_{hkl} = \bar{C}_{hk0} (1 + q_1 z + q_2 z^2), \quad (9.6)$$

where q_1 and q_2 are two parameters depending on the anisotropic elastic constants of the crystal and the type of dislocation slip system. $z = (2/3)(l/ga)^2$, where a is the lattice constant in the basal plane and g is the magnitude of the diffraction vector. \bar{C}_{hk0} is the average dislocation contrast factor for reflections $hk0$. The theoretical values of \bar{C}_{hk0} , q_1 and q_2 for the eleven possible slip systems in the most common hexagonal materials have been calculated according to the work of Kuzel and Klimanek (1988), and listed in Dragomir and Ungár (2002) and also in chapter 3. Each of the eleven slip systems has different theoretical values of \bar{C}_{hk0} , q_1 and q_2 parameters, therefore the evaluation of the experimental values of q_1 and q_2 enables the determination of the prevailing dislocation slip systems in the specimen. The eleven dislocation slip systems can be classified into three groups based on their Burgers vectors:

$$b_1 = \frac{1}{3} \langle \bar{2}110 \rangle (\langle a \rangle \text{ type}),$$

$$b_2 = \langle 0001 \rangle (\langle c \rangle \text{ type}) \text{ and}$$

$$b_3 = \frac{1}{3} \langle \bar{2}113 \rangle (\langle c+a \rangle \text{ type}).$$

There are 4, 2 and 5 slip systems in the $\langle a \rangle$, $\langle c \rangle$ and $\langle c+a \rangle$ Burgers vector groups, respectively. A computer program was elaborated in order to determine the distribution of dislocations among the different slip systems from the measured values of q_1^m and q_2^m (Máthis, Nyilas, Axt, Dragomir, Ungár, & Lukác, 2004). In this procedure those dislocation populations are determined which yield the same hkl dependence of line broadening as obtained from the experiment. In the case of dislocations the mean-square-strain, which determines the peak breadth, can be expressed as (Wilkins, 1970):

$$\langle \varepsilon_{g,L}^2 \rangle \cong \frac{\rho \bar{C}_{hkl} b^2}{4\pi} f(\eta), \quad (9.7)$$

Practical Applications of X-Ray Line Profile Analysis

where

$$\eta = \frac{1}{2} \exp\left(-\frac{1}{4}\right) \frac{L}{R_e^*}, \quad (9.8)$$

and ρ , b and R_e^* are the density, the modulus of Burgers vector and the effective outer cut-off radius of dislocations, respectively. The function $f(\eta)$ is referred to as Wilkens function and given in Equations (3.40)-(3.41) in chapter 3. Equation (9.7) shows that the variation of line broadening with the orientation of diffraction vector is determined by \bar{C}_{hkl} . Making the experimental value of $\bar{C}_{hkl} b^2$ equal to the theoretical value calculated by averaging for the eleven slip systems, the following equation is obtained:

$$\bar{C}_{hkl}^m \left(1 + q_1^m z + q_2^m z^2\right) b_m^2 = \sum_{i=1}^{11} f_i \bar{C}_{hkl}^i \left(1 + q_1^i z + q_2^i z^2\right) b_i^2, \quad (9.9)$$

where letter “ m ” indicates the values obtained from the measured profile, “ i ” denotes the theoretical values calculated for the i^{th} slip system and f_i is the fraction of dislocations in the the i^{th} slip system. The polynomials in the two sides of Equation (9.9) give the same values, if the coefficients of the terms with the same degrees are equal. This condition yields the following equations:

$$q_1^m = \frac{\sum_{i=1}^{11} f_i \bar{C}_{hk0}^i b_i^2 q_1^i}{\sum_{i=1}^{11} f_i \bar{C}_{hk0}^i b_i^2},$$

$$q_2^m = \frac{\sum_{i=1}^{11} f_i \bar{C}_{hk0}^i b_i^2 q_2^i}{\sum_{i=1}^{11} f_i \bar{C}_{hk0}^i b_i^2}, \quad (9.10)$$

$$\sum_{i=1}^{11} f_i = 1.$$

There is no equation for \bar{C}_{hk0}^m since it is not an independent parameter in the evaluation of line profiles as \bar{C}_{hk0}^m is multiplied with the dislocation density in Equation (9.7). The eleven values of f_i cannot be determined from the three formulas in Equation (9.10), therefore additional restrictions are made for f_i . It is assumed that in each Burgers vector group the non-zero fractions are equal. This assumption reduces the number of variables to three, which are denoted by f_a, f_c and f_{c+a} . The computer program written for the evaluation of Burgers vector population in hexagonal materials (referred to as *Hexburger*)

first selects some slip systems from $\langle a \rangle$ dislocation group and for these slip systems the weights are f_a . For other slip systems in this group the weights are zero. This procedure is also carried out for $\langle c \rangle$ and $\langle c+a \rangle$ Burgers vector groups where the non-zero weights are f_c and f_{c+a} , respectively. Inserting the theoretical values of \overline{C}_{hk0}^i , b_i , q_1^i and q_2^i into Equation (9.10), the values of f_a , f_c and f_{c+a} are determined. If these fractions have positive values the program stores them as one of the possible solutions. The number of the possible selections from the dislocation slip systems equals $(2^4-1)(2^2-1)(2^5-1)=1395$. Finally, the positive solutions for the weights can be averaged for each slip system, leading to the fractions of the eleven dislocation types. The fractions of the three Burgers vector groups, h_a , h_c and h_{c+a} , are obtained by the summation of the fractions of the related slip systems. For the sake of clarity, an example for the determination of the fractions of slip systems using the method *Hexburger* is shown in Figure 2. It should be noted that software *Hexburger* gives directly the solutions for h_a , h_c and h_{c+a} in a file for each selection of slip systems. Then, f_a , f_c and f_{c+a} can be determined by dividing h_a , h_c and h_{c+a} with the number of slip systems with non-zero weights in $\langle a \rangle$, $\langle c \rangle$ and $\langle c+a \rangle$ Burgers vector groups, respectively. It is emphasized that the procedure described above is worked out for non-textured polycrystalline hexagonal materials. In practice, the line profile evaluation directly yields $\overline{\rho C}_{hk0}^m$, q_1^m and q_2^m . Usually, in the fitting procedures (e.g. in CMWP, see chapter 6) a preliminary value for \overline{C}_{hk0}^m is assumed and the evaluation gives a first approximation for ρ , since its value depends on \overline{C}_{hk0}^m . Then, the Burgers vector population should be determined e.g. by the method described above, which results in the precise value of \overline{C}_{hk0}^m . Finally, this parameter is used for obtaining the exact value of the dislocation density.

Figure 2. Schematic picture illustrating the determination of the fractions of dislocation types for a particular selection of slip systems in hexagonal materials using the method *Hexburger*. The numbers 1 and 0 indicate the selected and non-selected slip systems, respectively. The notations of the eleven dislocation slip systems are explained in Figure 11 and Table 2 in Chapter 3.

	BE	PrE	PyE	S1	Pr2E	S3	Pr3E	Py2E	Py3E	Py4E	S2
selection:	1	0	0	1	0	1	1	1	0	1	0
fraction:	f_a	0	0	f_a	0	f_c	f_{c+a}	f_{c+a}	0	f_{c+a}	0
	$\underbrace{\hspace{10em}}$ $\langle a \rangle$ -type				$\underbrace{\hspace{4em}}$ $\langle c \rangle$ -type		$\underbrace{\hspace{15em}}$ $\langle c+a \rangle$ -type				
fraction:	$h_a = \sum f_a = 2f_a$				$h_c = \sum f_c = f_c$		$h_{c+a} = \sum f_{c+a} = 3f_{c+a}$				

Practical Applications of X-Ray Line Profile Analysis

If the program *Hexburger* does not give any positive solution for h_a , h_c and h_{c+a} , another method should be used for the analysis of the prevailing dislocation slip systems which can take into account the experimental error of parameters q_1^m and q_2^m . This procedure is referred to as *b2C* and described in details below (Ungár, Castelnau, Ribárik, Drakopoulos, Bechade, Chauveau, Snigirev, Snigireva, Schroer, & Bacroix, 2007). In each slip system selection, the weights (the values of f_i) for the activated slip systems is equal to $1/N_A$, where N_A is the number of the slip systems with non-zero weights, i.e. $0 < N_A < 11$. f_i is considered to be zero by definition for the non-activated slip systems. Then, the fractions of the three three Burgers vector types are given as:

$$h_a = \frac{N_A^a}{N_A}, \quad h_c = \frac{N_A^c}{N_A}, \quad h_{c+a} = \frac{N_A^{c+a}}{N_A}, \quad (9.11)$$

where N_A^a , N_A^c and N_A^{c+a} are the number of the activated slip systems in $\langle a \rangle$, $\langle c \rangle$ and $\langle c+a \rangle$ Burgers vector groups, respectively, and $N_A^a + N_A^c + N_A^{c+a} = N_A$. For the sake of clarity, an example for the determination of the fractions of slip systems using the method *b2C* is shown in Figure 3. The fundamental difference between methods *Hexburger* and *b2C* is that in the latter one the non-zero fractions for all Burgers vector groups are equal, while in the former procedure the fractions of slip systems in the various Burgers vector groups may be different. In the method *b2C* for a given selection of slip systems the fractions h_a , h_c and h_{c+a} obtained by Equation (9.11) are used to determine the calculated values of q_1^{cal} and q_2^{cal} . Then, these values are compared with the measured parameters q_1^m and q_2^m .

Figure 3. Schematic picture illustrating the determination of the fractions of dislocation types for a particular selection of slip systems in hexagonal materials using the method b2C. The numbers 1 and 0 indicate the selected and non-selected slip systems, respectively. The notations of the eleven dislocation slip systems are explained in Figure 11 and Table 2 in Chapter 3.

	BE	PrE	PyE	S1	Pr2E	S3	Pr3E	Py2E	Py3E	Py4E	S2
selection:	1	0	0	1	0	1	1	1	0	1	0
fraction:	$\frac{1}{N_A}$	0	0	$\frac{1}{N_A}$	0	$\frac{1}{N_A}$	$\frac{1}{N_A}$	$\frac{1}{N_A}$	0	$\frac{1}{N_A}$	0
	$N_A = 6, N_A^a = 2$				$N_A = 6, N_A^c = 1$		$N_A = 6, N_A^{c+a} = 3$				
	$\langle a \rangle$ -type				$\langle c \rangle$ -type		$\langle c+a \rangle$ -type				
fraction:	$h_a = \frac{N_A^a}{N_A} = \frac{2}{6}$				$h_c = \frac{N_A^c}{N_A} = \frac{1}{6}$		$h_{c+a} = \frac{N_A^{c+a}}{N_A} = \frac{3}{6}$				

Since these measured values have experimental errors, the comparison has to be carried out by introducing tolerances (Ungár, Castelnau, Ribárik, Drakopoulos, Bechade, Chauveau, Snigirev, Snigireva, Schroer, & Bacroix, 2007). A given slip system combination was considered valid if both q_1^{cal} and q_2^{cal} satisfied the following two tolerance conditions simultaneously:

1. $q_1^m - \Delta q^{abs} < q_1^{cal} < q_1^m + \Delta q^{abs}$ and $q_2^m - \Delta q^{abs} < q_2^{cal} < q_2^m + \Delta q^{abs}$, if $|q_1^m| < 1$ and $|q_2^m| < 1$
2. $1 - \Delta q^{rel} < \frac{q_1^{cal}}{q_1^m} < 1 + \Delta q^{rel}$ and $1 - \Delta q^{rel} < \frac{q_2^{cal}}{q_2^m} < 1 + \Delta q^{rel}$, if $|q_1^m| \geq 1$ and $|q_2^m| \geq 1$,

where Δq^{abs} and Δq^{rel} are the absolute and relative tolerances which should be specified in the evaluation procedure. The reasonable values of tolerances are usually between 0.1 and 0.3. Finally, the values of h_a , h_c and h_{c+a} are obtained for a number of valid slip system combinations.

Experiments have shown that the majority of dislocations (~90%) in hexagonal materials have $\langle a \rangle$ or $\langle c+a \rangle$ -type Burgers vector. The determination of the fractions of $\langle a \rangle$ and $\langle c+a \rangle$ dislocations is facilitated by the opposite signs of the broadening effects of $\langle a \rangle$ and $\langle c+a \rangle$ edge dislocations on many reflections. This means that for a given reflection $\langle a \rangle$ and $\langle c+a \rangle$ edge dislocations cause broader and narrower breadths, respectively, relative to the width of reflections $hk0$. Figures 4 and 5 show this effect

Figure 4. The theoretical dislocation contrast factors of $\langle a \rangle$ -type dislocations for the first nineteen reflections of Mg as a function of the length of the diffraction vector, g . The contrast factors are normalized with the value for reflections $hk0$.

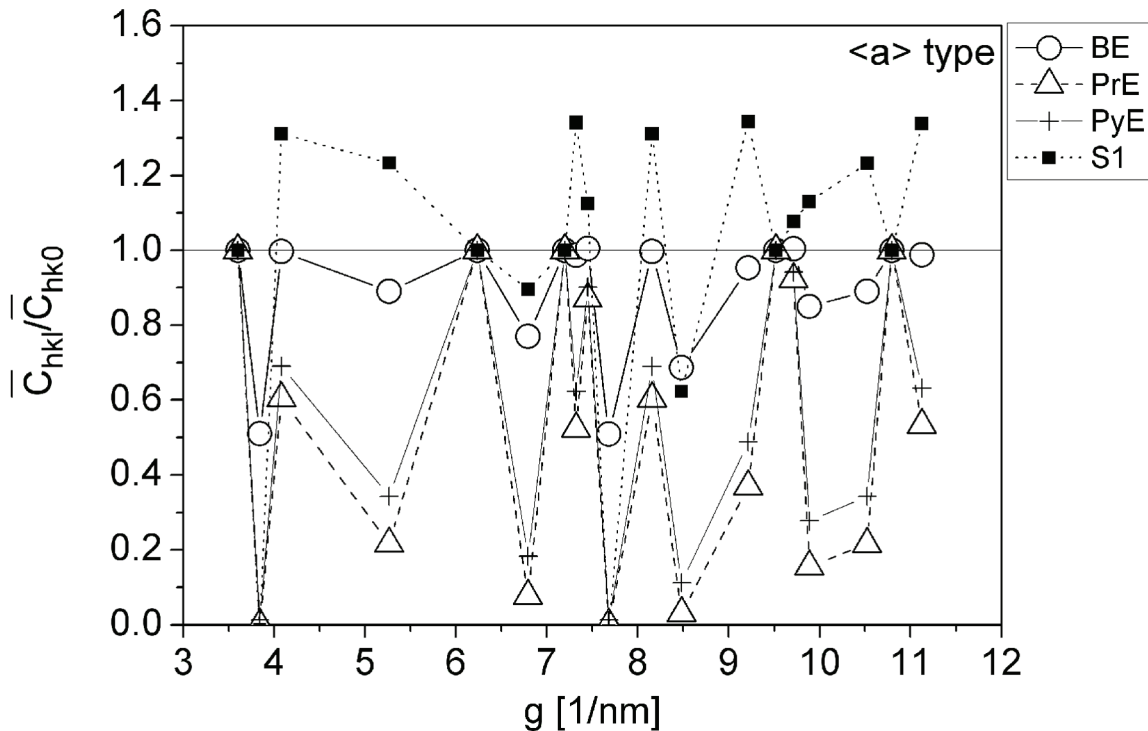
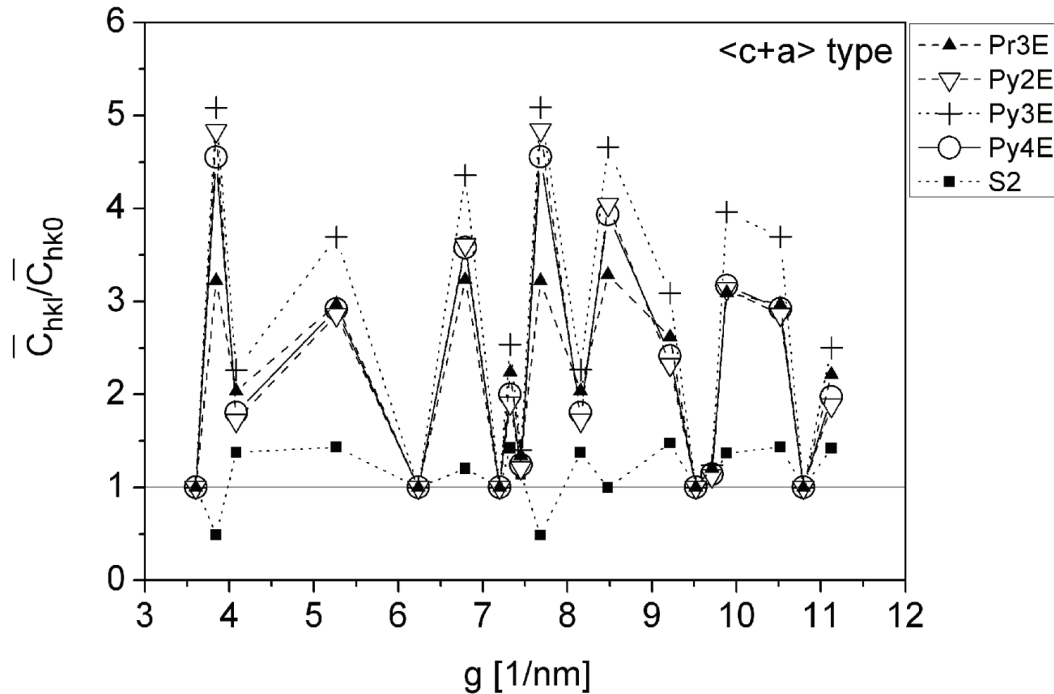


Figure 5. The theoretical dislocation contrast factors of $\langle c+a \rangle$ -type dislocations for the first nineteen reflections of Mg as a function of the length of the diffraction vector, g . The contrast factors are normalized with the value for reflections $hk0$.



on Mg where the theoretical contrast factors for the first nineteen reflections are plotted as a function of g . It is noted that due to the very similar contrast effects of PrE and PyE dislocations, the ratio of their fractions is uncertain, as determined by *Hexburger* or *b2C* method. The same holds also for Py2E and Py4E dislocation types. In the next section, some results obtained on the dislocation structures in hexagonal materials by X-ray line profile analysis are summarized.

Severe plastic deformation (SPD) procedures are often applied in order to obtain ultrafine-grained (UFG) or nanocrystalline microstructure in hexagonal metals, such as commercially pure Ti (Gubicza, Dragomir, Ribárik, Baik, Zhu, Valiev, & Ungár, 2003; Gubicza, Dragomir, Ribárik, Zhu, Valiev, & Ungár, 2003; Gubicza, Nam, Balogh, Hellmig, Stolyarov, Estrin, & Ungár, 2004; Mingler, Stolyarov, Zehetbauer, Lacom, & Karnthaler, 2006; Zeipper, Zehetbauer, & Holzleithner, 2005; Zhu, Huang, Gubicza, Ungár, Wang, Ma, & Valiev, 2003) and AZ91 Mg alloy (Máthis, Gubicza, & Nam, 2005). In the case of hexagonal materials SPD processes are generally carried out at elevated temperatures due to the rigidity of the specimens at room temperature. In commercially pure Ti specimen processed by eight passes of equal channel angular pressing (ECAP) at 400–450°C, the relative fractions of $\langle a \rangle$, $\langle c \rangle$ and $\langle c+a \rangle$ -type dislocations were 62%, 4% and 34%, respectively (Zhu, Huang, Gubicza, Ungár, Wang, Ma, & Valiev, 2003). The abundance of $\langle a \rangle$ -type dislocations besides the $\langle c \rangle$ - and $\langle c+a \rangle$ -type dislocations has also been found for other bulk hexagonal nanomaterials, e.g for sintered WC (Gubicza, Ribárik, Goren-Muginstein, Rosen, & Ungár, 2001) and plastically deformed Mg alloys (Máthis, Gubicza, & Nam, 2005; Máthis, Nyilas, Axt, Dragomir, Ungár, & Lukác, 2004). This observation can be attributed to the lowest formation energy of these dislocations due to their smallest Burgers vector among the three

Burgers vector groups. Before ECAP-processing of AZ91 magnesium alloy the relative fractions of $\langle a \rangle$, $\langle c \rangle$ and $\langle c+a \rangle$ dislocations were about 80%, 10% and 10%, respectively. The ECAP procedure at 270°C yielded changes of the fractions of $\langle a \rangle$, $\langle c \rangle$ and $\langle c+a \rangle$ Burgers vector groups to 57%, 1% and 43%, respectively (Máthis, Gubicza, & Nam, 2005). The relatively high fraction of $\langle c+a \rangle$ dislocations in deformed Mg and Ti can be attributed to the high temperature of straining. Theoretical calculations and TEM observations for hexagonal metallic materials suggest the activation of $\langle c+a \rangle$ dislocations by strong deformation at elevated temperatures (Yoo, 1981). At room temperature the critical resolved shear stress for pyramidal $\langle c+a \rangle$ dislocations is about five times larger than that for basal slip, but this value is reduced when the deformation temperature is enhanced. The AZ91 magnesium alloy processed by ECAP at 270°C was further deformed by tension at different temperatures (Máthis, Gubicza, & Nam, 2005). At relatively low temperature the dominance of $\langle a \rangle$ type dislocations can be established. At high temperatures, e.g. at 300°C, the relative fraction of $\langle a \rangle$ Burgers vector type decreased and the relative fraction of $\langle c+a \rangle$ dislocations increased. This result is in agreement with the general observation that $\langle c+a \rangle$ dislocations are activated in hexagonal metals during plastic deformation at elevated temperatures. The heat-treatment of severely deformed Ti resulted in both the decrease of the dislocation density and the change of the fractions of the different slip systems (Gubicza, Nam, Balogh, Hellmig, Stolyarov, Estrin, & Ungár, 2004). As the temperature increased the relative fraction of the $\langle c+a \rangle$ -type dislocations decreased down to about 2%, indicating that these dislocations disappeared faster than $\langle a \rangle$ or $\langle c \rangle$ -type dislocations. This can be explained by the fact that $\langle c+a \rangle$ -type dislocations have larger Burgers vector and consequently higher formation energy than other two types.

INVESTIGATION OF TWIN BOUNDARY TYPES IN HEXAGONAL CRYSTALS

Unlike face centered cubic (fcc) crystals, in hexagonal close-packed (hcp) materials the planes of twin faults differ from the close packed crystallographic planes. In hcp crystals the shear of the crystal during twinning occurs mainly on $\{101\}$, $\{112\}$, $\{102\}$ and $\{111\}$ planes in $\langle 10\bar{2} \rangle$, $\langle 11\bar{3} \rangle$, $\langle 10\bar{1} \rangle$ and $\langle \bar{1}\bar{1}6 \rangle$ directions, respectively. The first two and the last two twins are referred to as compressive and tensile twins, respectively (Chun, Yu, Semiatin, & Hwang, 2005; Paton & Backofen, 1970). As an example, the twin boundary on $\{102\}$ plane is illustrated in Figure 2 in Chapter 4. As it was discussed in chapter 6, extended Convolutional Multiple Whole Profile (eCMWP) fitting procedure is capable to determine the twin fault probability in hcp materials from line profiles. However, the software can not handle two or more types of twin fault simultaneously, therefore the user should decide which one from the four twin fault types is included in the microstructure model of fitting. After the selection of the twin type, the related parameter file is used in the fitting procedure. Additional option is that the parameter file is prepared for the weighted average of two, three or four twin fault types. For instance, Balogh, Tichy, and Ungár (2009) has studied the prevailing twin faults in high-purity Ti specimen deformed in compression to 20% reduction at room temperature. The line profile evaluation was carried out by the eCMWP procedure including the four twin fault types. The evaluation was carried out by systematically choosing the different combinations of the possible twin systems. First, each twin family was considered separately, then two twin families were combined pairwise with equal weights in each possible combination and finally all four twin families were combined with equal weights. The combination corresponding to the best pattern fitting was considered to be the prevailing twin types. The smallest sum of squared dif-

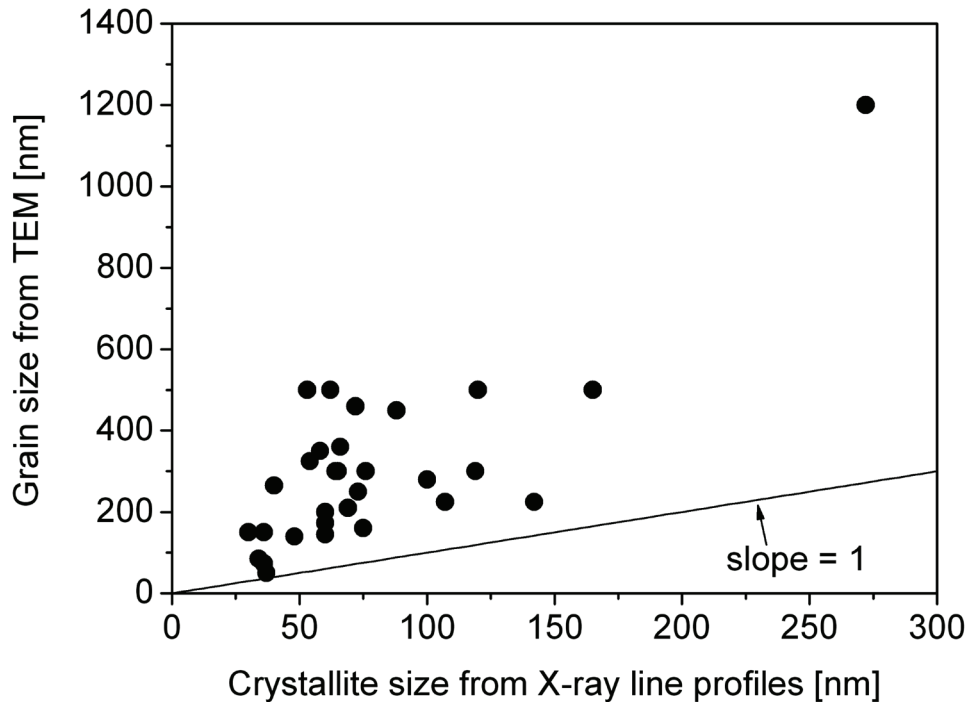
ferences between the experimental and fitting intensity values was reached when {101} and {112} compressive twin families with equal weights was assumed in the microstructure (Balogh, Tichy, & Ungár, 2009). The twin fault probability was about 2%. Similar evaluation procedure for the twin types was performed in the case of a commercial purity Ti rolled to a reduction of 10% in a single pass at 993 K (Ungár, Glavicic, Balogh, Nyilas, Salem, Ribárik, & Semiatin, 2008). The sample was quenched in water to room temperature in order to preserve the defect structure formed at elevated temperature. {102} tensile and {112} compressive twin families were observed with relatively low probabilities of ~0.07% (Balogh, Tichy, & Ungár, 2009). The twin boundary type was also investigated in Mg specimens of 99% purity deformed by tension up to fracture at different temperatures ranging from room temperature to 573 K (Balogh, Tichy, & Ungár, 2009). The systematic analysis of the different twin families and their combinations revealed that in the Mg specimens the dominant twin family is {111}, regardless the deformation temperature. However, the twin fault probability varied with the applied temperature. The highest twin boundary probability of about 0.3% was observed after deformation at room temperature which decreased to ~0.1% with increasing temperatures up to 573 K. Simultaneously, $\langle c+a \rangle$ -type dislocations are activated in accordance with TEM observations discussed in the previous section.

INTERPRETATION OF CRYSTALLITE SIZE OBTAINED BY LINE PROFILE ANALYSIS

The crystallite size (or coherently scattering domain size) determined by X-ray line profile analysis often differs from the grain or particle size obtained by scanning electron microscopy (SEM) or TEM (Ungár, Victoria, Marmy, Hanák, & Szenes, 2000; Ungár, Gubicza, Ribárik, & Borbély, 2001; Gubicza, Dragomir, Ribárik, Baik, Zhu, Valiev, & Ungár, 2003; Zhu, Huang, Gubicza, Ungár, Wang, Ma, & Valiev, 2003; Samadi Khoshkhoo, Scudino, Thomas, Gemming, Wendrock, & Eckert, 2013). Usually, the crystallite size determined from diffraction profiles is equal or smaller than the size value determined by microscopic methods. In the case of plastically deformed bulk metals and alloys, the grain size is 2-10 times larger than the crystallite size, as illustrated in Figure 6. This phenomenon can be attributed to the fact that the crystallites are equivalent to the domains in the microstructure which scatter X-rays coherently. As the coherency of X-rays breaks even if they are scattered from volumes having quite small misorientations ($1-2^\circ$), the crystallite size corresponds rather to the subgrain size in severely deformed microstructures (Ungár, Schafler, & Gubicza, 2009). The subgrains are usually separated by low angle grain boundaries consisting of dislocations with the same sign.

Besides low angle grain boundaries, dipolar dislocation walls resulting in zero misorientation between the separated regions (cells) can also break down coherency of X-ray scattering (Ungár, Tichy, Gubicza, & Hellmig, 2005). Dipolar dislocation walls are shown schematically in chapter 3. These walls do not cause tilt or twist between the separated cells (Wilkens, Ungár, & Mughrabi, 1987), however the lattice planes in these cells are shifted relative to each other (Ungár, Tichy, Gubicza, & Hellmig, 2005). This shift varies randomly from cell to cell between 0 and $b/2$, where b is the magnitude of Burgers vector of dislocations. The shifts of the lattice planes yield uncorrelated phase shifts in the X-rays scattered by the different cells. This means that there is no coherency between the X-rays scattered by the volumes separated by the dipolar walls, and the line broadening is determined by the average cell size instead of the larger grain size (Ungár, Schafler, & Gubicza, 2009). As a consequence, the crystallite size distribution

Figure 6. The mean grain size versus the average crystallite size determined by TEM and X-ray line profile analysis, respectively, for metals and alloys processed by SPD methods



obtained by X-ray line profile analysis corresponds to the size distribution of subgrains or dislocation cells in the materials where these boundaries exist. Figure 7 illustrates the good agreement between the subgrain and crystallite size distributions determined for severely deformed commercial purity Ti by TEM and X-ray line profile analysis, respectively. A similar result was obtained for Cu powder after either cryomilling for 3 h or subsequent consolidation by hot extrusion (Samadi Khoshkhou, Scudino, Thomas, Gemming, Wendrock, & Eckert, 2013). Combined TEM, SEM and X-ray line profile analysis investigations revealed that in both samples line profile analysis yielded the size distribution of subgrains. For metallic materials processed in either bulk or powder form without the application of severe plastic deformation (e.g. by condensation or deposition methods) the crystallite size obtained by X-ray line profile analysis agrees well with the grain or particle size determined by TEM due to the lack of subgrain structure.

For special dislocation boundaries the crystallite size determined by X-ray line profile analysis may differ from the spacing between these boundaries. Wilkens (1979) has shown by theoretical calculations that in the case of periodically distributed low-angle grain boundaries the crystallite size is larger than the spacing between the boundaries, D_B , by a factor of about two when the spacing between the boundaries is close to the spacing between the dislocations within the boundaries, D_d (see Figure 8). In periodic low-angle grain boundaries the adjacent boundaries consist of dislocations with opposite sign. The crystallite size converges to the boundary spacing with increasing the ratio D_B/D_d . When this ratio is larger than ten, the deviation of the apparent crystallite size from D_B is less than 5% (Wilkens, 1979). It is noted that the crystallite size was obtained from line profiles with diffraction vectors perpendicu-

Figure 7. The subgrain size distribution determined by TEM and the crystallite size distribution obtained by X-ray line profile analysis for Ti processed by 8 ECAP passes

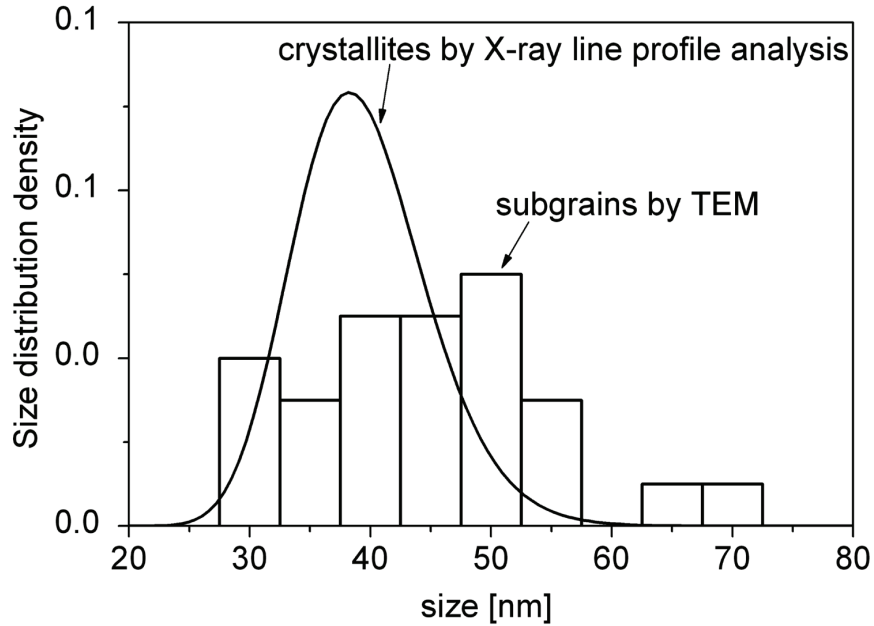
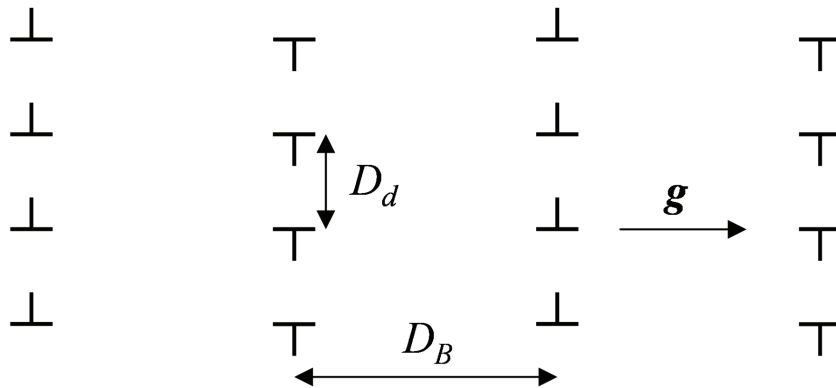


Figure 8. Periodically distributed low-angle grain boundaries consisting of dislocations. Vector \mathbf{g} indicates the diffraction vector perpendicular to the boundaries.

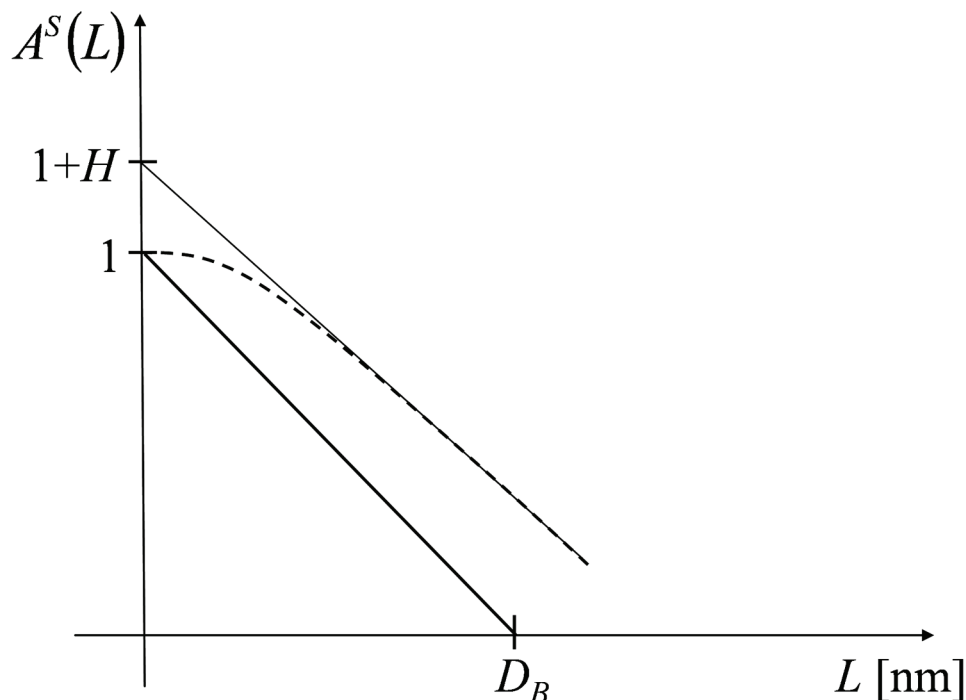


lar to the boundaries by Warren-Averbach analysis (see chapter 6). The larger apparent crystallite size compared to the boundary spacing is accompanied by a negative curvature on the size Fourier transform

$$\left(\frac{\partial^2 A^s}{\partial L^2} < 0\right)$$

for small values of Fourier variable, L , as obtained by the Warren-Averbach method (see Figure 9). This phenomenon is referred to as “hook” effect (Wilkins, 1979). Due to the negative curvature a linear

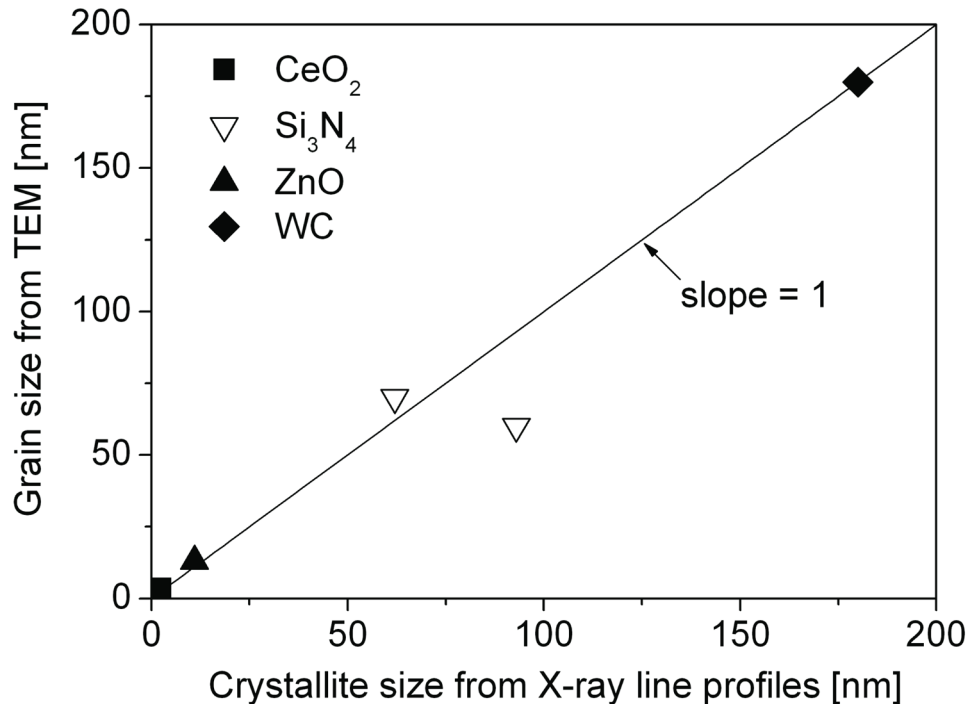
Figure 9. Illustration of the “hook” effect on the normalized size Fourier transform, A^S (dashed line), for small values of Fourier variable (L) in the case of low-angle grain boundaries with small ratio of D_B/D_d . Due to the negative curvature a linear extrapolation back to the vertical axis (thin solid line) yields an intersection $1+H$ ($H>0$) instead of 1. If the apparent crystallite size were equal to the boundary spacing D_B , the tangent at the beginning of the curve would be the thick solid line.



extrapolation back to the vertical axis yields an intersection $1+H$ ($H>0$) instead of 1, as illustrated in Figure 9. H measures the strength of the “hook” effect. H increases with decreasing D_B/D_d and reaches 16% for $D_B/D_d=1$. The “hook” effect is caused by the particular properties of the strain field around low-angle grain boundaries containing dislocations. There is a smooth change in crystallographic orientation within a boundary transition layer with the thickness of $2D_d$, therefore the boundary does not interrupt coherency, resulting in larger crystallite size (Wilkens, 1979). It is also noted that the mean-square-strain determined from the Warren-Averbach analysis is significantly smaller and decreases with increasing L more rapidly than the values calculated theoretically from the strain fields of dislocations in the boundaries. Obviously, these anomalies are reduced with increasing D_B/D_d . It should be noticed that the “hook” effect may also be caused by the subtraction of an overestimated background (Warren, 1990). For overlapping peaks the background may be determined at higher level than the true one, which yields too small value of A^S at $L=0$ (it is equivalent to the peak area).

Due to the ionic and covalent bonding in ceramic materials, the critical resolved shear stress for dislocation motion is large. Therefore, dislocations do not form subgrain boundaries or dipolar walls in ceramics during the processing of these materials. As a consequence, the crystallite size determined by X-ray line profile analysis usually agrees with the grain or particle size obtained by TEM for ceramic powders or sintered materials, respectively, as shown in Figure 10. This means that the grains or particles in the bulk or powder ceramic materials, respectively, are single crystals, i.e. in contrast with metals

Figure 10. The mean grain size versus the average crystallite size determined by TEM and X-ray line profile analysis, respectively, for ceramic materials



they are not divided into smaller domains, e.g. by dislocation cell-walls (Gubicza & Ungár, 2007). In the case of ceramic powders this observation can also be supported by complementary specific surface area measurements. For instance, the area-weighted mean crystallite size obtained by X-ray line profile analysis for a silicon nitride powder produced by silicon nitridation and subsequent milling, 62 ± 5 nm, agreed well with the area weighted mean particle size, 71 ± 5 nm, calculated from the specific surface area using the Brunauer-Emmett-Teller (BET) method (Gubicza, Szépvölgyi, Mohai, Zsoldos, & Ungár, 2000). The crystallite size distribution determined by X-ray peak profile analysis was also in a very good agreement with the particle size distribution obtained from TEM micrographs. Another Si₃N₄ powder was prepared by gas-phase synthesis of silicon-tetrachloride and ammonia in thermal plasma reactor and post-crystallization at 1500°C for 2 h (Gubicza, Szépvölgyi, Mohai, Zsoldos, & Ungár, 2000). It was found that the mean crystallite size obtained by line profile analysis, 93 ± 5 nm, was in good agreement with the particle size determined by BET method 94 ± 5 nm. It should be noted that for this powder the particle size obtained by TEM was smaller than the crystallite size obtained from line profile analysis. This is an unusual phenomenon among the comparative studies of X-ray and TEM sizes since in general the crystallite size determined by X-ray diffraction is equal or smaller than the particle size established by TEM. The phenomenon can be explained by a considerable fraction of amorphous particles in the Si₃N₄ powder prepared by gas-phase synthesis. In this powder the amorphous particles have smaller size than that for the crystalline particles. In multiple-phase ceramic materials where the particles consists of crystallites of different phases, the particle size can be larger than the crystallite size, as shown in the case of zirconia ceramics (Lin & Duh, 1997). In ceramic powders containing amorphous fraction the crystallite size can be smaller or higher than the particle size.

COMPARISON OF LATTICE DEFECT DENSITIES OBTAINED BY PEAK PROFILE ANALYSIS AND MICROSCOPY

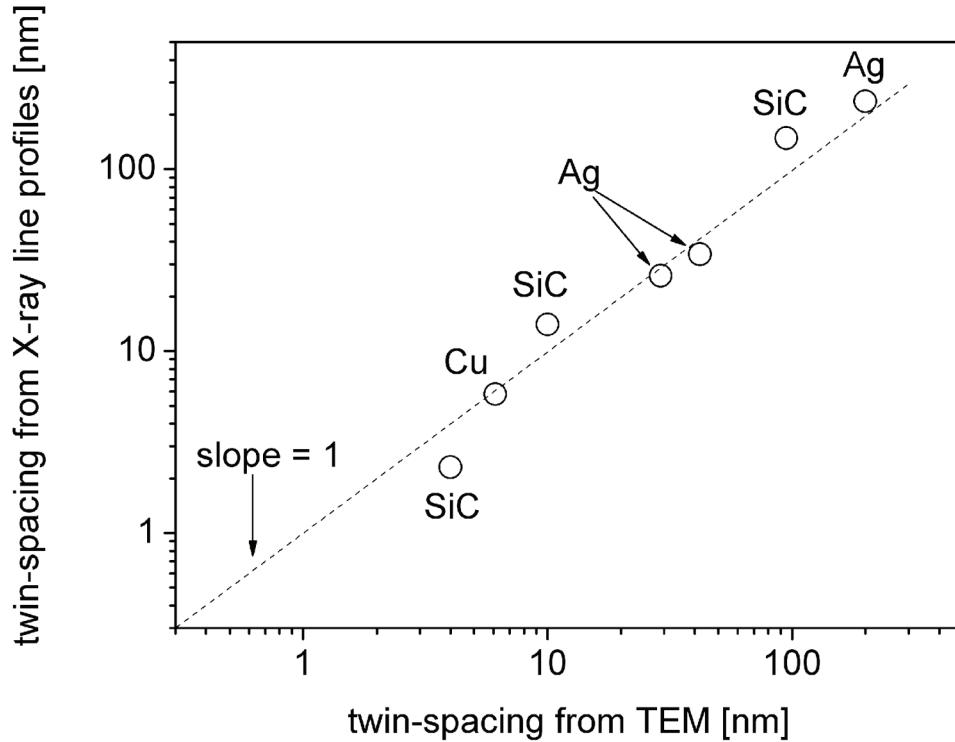
In the study of microstructure both direct and indirect methods, such as TEM and X-ray line profile analysis, respectively, can be applied, therefore their comparison is useful from practical viewpoint. In the case of peak profile analysis the sample preparation easier than in TEM, and additionally the former method is non-destructive. The most important advantage of TEM is that the microstructure can be investigated directly, while a model of the microstructure is necessary to evaluate X-ray line profiles. However, peak profile analysis gives the parameters of the defect structure with a better statistics since X-ray diffraction usually examines 10^3 - 10^5 larger sample volume than that studied by TEM. It is beneficial in the case of TEM that this method can investigate the grain and particle sizes for both small and large values. At the same time, instrumental broadening in X-ray line profile analysis yields an upper detection limit for the crystallite size which is 400-800 nm, depending on the wavelength distribution of X-rays and the instrument geometry. It should be noted that for some materials line profile analysis and TEM give complementary information about the dimension of the microstructure units. For instance, in the case of plastically deformed bulk metals X-ray peak profile analysis and TEM yield the subgrain or cell size and the grain size, respectively, as discussed above. Regarding the study of lattice defect, line profile analysis and TEM usually can be applied successfully for large and low defect densities, respectively, although these regimes usually overlap. For instance, the dislocation density can only be determined by X-ray line profile analysis if it is larger than 10^{12} - 10^{13} m⁻², while the counting of individual dislocations in TEM images is impossible if their density exceeds $\sim 5 \times 10^{14}$ m⁻². It is noted that high-resolution TEM (HRTEM) can provide the local dislocation density even for its very large values, but with a much worse statistics compared to X-ray diffraction peak profile analysis. Furthermore, the local dislocation density may strongly deviate from the value averaged for a larger volume. For instance, in the case of severely deformed metals the dislocation density in subgrain and grain boundaries determined by HRTEM is often two orders of magnitude larger than the average value obtained from X-ray line profiles (Zhu, Huang, Gubicza, Ungár, Wang, Ma, & Valiev, 2003).

The instrumental effect also yields a lower limit for the detectable value of the twin boundary probability, which is 0.02-0.1%, depending on the experimental conditions. Intermediate twin fault probability values can be determined by both X-ray line profile analysis and TEM. In order to compare the twin fault frequency determined from diffraction profiles with the direct observation performed by TEM, the twin fault probability can be transformed into the mean spacing between twin boundaries. For instance, in fcc crystals the mean twin-spacing (d_{twin}) can be obtained from the twin fault probability (β_t) as:

$$d_{twin} = \frac{100 \cdot d_{111}}{\beta_t}, \quad (9.12)$$

where d_{111} is the distance between the neighboring {111} planes. The mean twin-spacing values obtained by X-ray line profile analysis and TEM show good agreement within the experimental error, as illustrated in Figure 11. However, X-ray diffraction peak profile analysis and TEM usually provide different aspects of the microstructure, therefore they are suggested to use as complementary methods.

Figure 11. The correlation between the mean twin-spacing values determined by TEM and from the X-ray line profiles for Ag and SiC samples



DETERMINATION OF VACANCY CONCENTRATION WITH THE HELP OF X-RAY LINE PROFILE ANALYSIS

During plastic deformation of metallic materials besides dislocations vacancies are also formed. The most important phenomenon resulting in vacancy production is the climb of edge dislocation segments. Similar to other lattice defects, vacancies also play a major role in controlling the hardening behavior and the ductility of metals (Zehetbauer, Stuewe, Vorhauer, Schafler, & Kohout, 2003; Zehetbauer, Kohout, Dubravina, Schafler, & Vorhauer, 2004), therefore the evolution of their concentration as a function of strain is a key issue. The vacancy concentration can be determined by positron annihilation spectroscopy (PAS). In severely deformed metallic materials the densities of dislocations and vacancies are so high that every positron is very quickly trapped at dislocations or vacancy clusters (referred to as saturated positron trapping). Therefore, the concentration of vacancies can only be evaluated from the PAS signal if the dislocation density is determined individually by X-ray line profile analysis. The ratio, I_2/I_1 , of the intensities of PAS signals corresponding to positrons trapped in vacancy clusters and at dislocations is directly proportional to the ratio of cluster concentration and dislocation density (Cizek, Janecek, Srba, Kuzel, Barnovska, Prochazka, & Dobatkin, 2011):

$$\frac{I_2}{I_1} = \frac{\nu_{VC}c_{VC}}{\nu_D\rho}, \quad (9.13)$$

where ν_{VC} , ν_D are the specific positron trapping rate to vacancy clusters and dislocations, respectively, c_{VC} is the vacancy cluster concentration and ρ is the dislocation density. For instance, the values of ν_{VC} , ν_D for Cu are 1.2×10^{14} at s^{-1} and $0.6 \times 10^{-4} m^2 s^{-1}$, respectively (Cizek, Janecek, Srba, Kuzel, Barnovska, Prochazka, & Dobatkin, 2011). Multiplying the cluster concentration with the number of vacancies in the clusters, which can be obtained from the positron lifetime, the total vacancy concentration can be calculated.

The vacancy concentration can also be determined by a combination of X-ray line profile analysis and residual electrical resistometry (RER) (Schafler, Steiner, Korznikova, Kerber, & Zehetbauer, 2005). The decrease of electrical resistivity during annealing of severely deformed samples is caused by the annihilation of lattice defects such as vacancies (vacancy clusters) and dislocations. The contribution of dislocations to resistivity can be estimated from the dislocation density determined by X-ray line profile analysis and the specific dislocation resistivity (e.g. $0.8 \times 10^{-25} \Omega m^{-3}$ for Cu (Watts, 1989)). Subtracting this contribution from the total decrease of resistivity, the vacancy concentration can be determined as the ratio of the remaining resistivity and the resistivity per unit vacancy concentration ($0.62 \times 10^{-4} \Omega cm$ for Cu (Wollenberger, 1983)).

The vacancy concentration can also be obtained by differential scanning calorimetry (DSC) with the help of line profile analysis (Schafler, Steiner, Korznikova, Kerber, & Zehetbauer, 2005). For plastically deformed materials usually a single exothermic peak is observed in DSC thermogram. The released heat is assumed to be a sum of the contributions of vacancies, dislocations and high-angle grain boundaries. The energy stored in dislocations (E_{disl}) in a unit mass can be determined from the dislocation density using the following relationship (Schafler, Steiner, Korznikova, Kerber, & Zehetbauer, 2005):

$$E_{disl} = A^* \frac{Gb^2\rho}{\rho_m} \ln \frac{1}{b\sqrt{\rho}}, \quad (9.14)$$

where G is the shear modulus, b is the magnitude of Burgers vector, ρ is the dislocation density, ρ_m is the mass density and A^* denotes a factor which depends on the edge/screw character of dislocations. The value of A^* is equal to $(4\pi)^{-1}$ and $(4\pi(1-\nu))^{-1}$ for screw and edge dislocations, respectively, where ν is Poisson's ratio. For cubic materials, the parameter q determined from X-ray line profile analysis describes the edge/screw character of the dislocations. In practice, the value of A^* is obtained from the experimentally determined q_{exp} and the theoretical values for edge and screw dislocations q_{edge} and q_{screw} , respectively, using a simple rule of mixtures (Gubicza, Dobatkin, Khosravi, Kuznetsov, & Lábár, 2011):

$$A^* = \frac{q_{exp} - q_{edge}}{q_{screw} - q_{edge}} \frac{1}{4\pi} + \frac{q_{screw} - q_{exp}}{q_{screw} - q_{edge}} \frac{1}{4\pi(1-\nu)}. \quad (9.15)$$

The interfaces between the grains can be classified as low- and high-angle grain boundaries (LAGBs and HAGBs, respectively). The LAGBs usually consist of dislocations and X-ray line profile analysis measures dislocations in both the boundaries and the interiors of the grains so that the contribution of LAGBs to the stored energy is incorporated in Equation (9.14). The energy of the HAGBs (E_{HAGB}) is given as (Humphreys & Hatherly, 2004):

Practical Applications of X-Ray Line Profile Analysis

$$E_{HAGB} = h^* \frac{3\gamma_{GB}}{d\rho_m}, \quad (9.16)$$

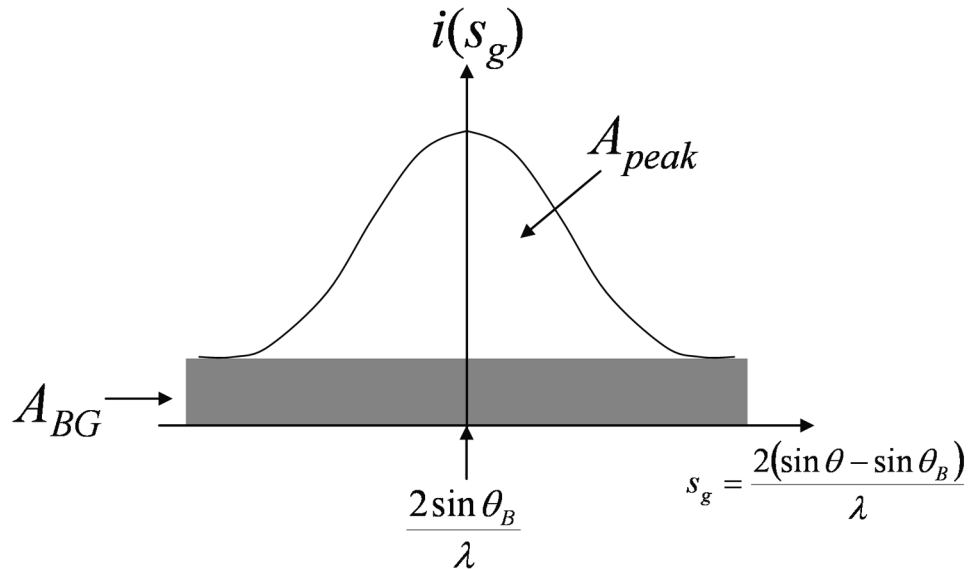
where γ_{GB} is the average HAGB energy, h^* is the fraction of HAGBs and d is the average grain size. The value of h^* can be obtained by electron backscatter diffraction (EBSD) experiments. Subtracting the sum of E_{disl} and E_{HAGB} from the released heat, the contribution of vacancies to stored energy is obtained which can be expressed from the vacancy concentration (c_v) as (Schafler, Steiner, Korznikova, Kerber, & Zehetbauer, 2005):

$$E_{vac} = e_{vac} c_v \frac{n_A}{M_m}, \quad (9.17)$$

where e_{vac} is the formation energy of a vacancy, n_A is Avogadro's number ($6 \times 10^{23} \text{ mol}^{-1}$) and M_m is the molar mass.

The diffuse scattering caused by crystals containing lattice defects has already been studied in details (Eckstein, 1945; Huang, 1947; Krivoglaz, 1969; Trinkaus, 1972). It was found that vacancies have a considerable contribution to the diffuse background scattering under X-ray diffraction peaks, therefore the ratio of the integrated background and the integrated peak intensities can be used for the determination of vacancy concentration after a calibration procedure (Ungár, Schafler, Hanák, Bernstorff, & Zehetbauer, 2007). This method was used for in-situ investigation of the evolution of vacancy concentration in high purity [001]-oriented Cu single crystal and a polycrystalline copper specimen with an average grain size of $\sim 80 \mu\text{m}$ during compression at a strain rate of $\sim 5 \times 10^{-5} \text{ s}^{-1}$ (Schafler, Simon, Bernstorff, Hanák, Tichy, Ungár, & Zehetbauer, 2005). The peak profiles were measured by synchrotron radiation. In the case of the initial undeformed single- and polycrystalline specimens only a very low intensity of the diffuse background was observed. However, the background intensity increased considerably with increasing strain. For the quantitative characterization of the relative intensity of the background scattering in the diffractogram, the ratio of the integrated intensities of the background and the diffraction peak, $R = A_{BG} / A_{peak}$, was used, as illustrated in Figure 12 (Ungár, Schafler, Hanák, Bernstorff, & Zehetbauer, 2005). The increase of the value of R with increasing strain was attributed to the increase of the concentration of vacancies and/or vacancy clusters. The value of R was transformed into vacancy concentration after a calibration procedure. For this purpose, the vacancy concentration was determined from the combination of X-ray line profile analysis and RER or DSC (Schafler, Steiner, Korznikova, Kerber, & Zehetbauer, 2005) and compared with the ratio R . After calibration the vacancy concentration were available for both single crystal and polycrystal Cu specimens in a wide range of strain. It was revealed that in the polycrystalline specimen the vacancy concentration increases much faster at small strain values and remains larger throughout the entire deformation range than the vacancy concentration for the single crystalline sample. This result is most probably caused by the larger vacancy accumulation in the grain boundary region compared to the grain interiors. From the diffraction peaks the dislocation density as a function of strain was also evaluated. Comparing conventional and severe plastic deformation (e.g. ECAP) the latter exhibits a much higher production rate of vacancies (Zehetbauer, Schafler, & Ungár, 2005). This effect is attributed to the enhancement of hydrostatic pressure component in SPD-processing

Figure 12. Schematic picture illustrating the determination of the integrated background and peak intensities, A_{BG} and A_{peak} , respectively



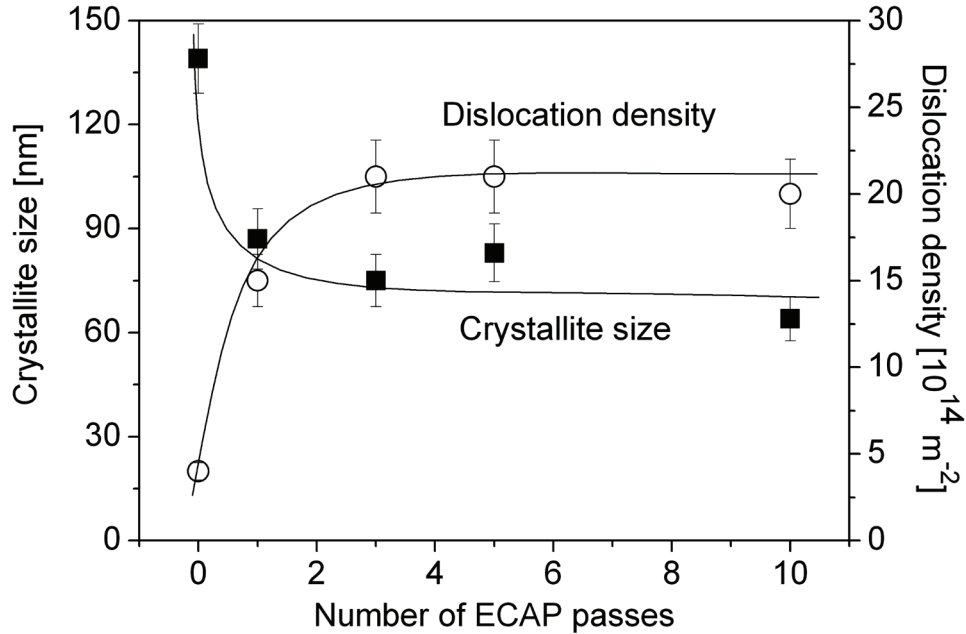
which impedes the diffusion of vacancies and thus their annihilation. It was found that the evolution of vacancy concentration was proportional to the increase of the dislocation density with increasing strain (Ungár, Schafler, Hanák, Bernstorff, & Zehetbauer, 2005).

DETERMINATION OF LATTICE DEFECT STRUCTURE IN ULTRAFINE-GRAINED AND NANOCRYSTALLINE MATERIALS

UFG and nanocrystalline materials can be processed by either “bottom-up” or “top-down” approaches (Gubicza, 2012). In the first case the materials are built up from individual atoms, molecules or their clusters (particles), such in electrodeposition or inert gas condensation. In the second case, the UFG microstructure is achieved by refinement of coarse-grained materials e.g. by SPD of bulk materials or by milling of powders.

SPD techniques are effective methods for producing bulk, porosity- and contamination-free UFG or nanostructured materials (Valiev & Langdon, 2006; Zhilyaev & Langdon, 2008). The high pressure applied during these procedures promotes the evolution of a high dislocation density in two ways: i) by impeding the vacancy migration that hinders the annihilation of dislocations and ii) by suppressing the cracking thereby keeping the integrity of the workpiece even at high strains. The most frequently used SPD procedure is ECAP that enables the elaboration of bulk UFG or nanomaterials with dimensions of several centimeters in all directions that is favorable in practical applications (Valiev & Langdon, 2006). One pass of ECAP corresponds to an equivalent strain value of about 1 (i.e. 100%). The imposed strain increases proportionally with the increase of the number of passes. The evolution of the dislocation density and the crystallite size determined by X-ray line profile analysis as a function of number of ECAP passes is illustrated in Figure 13 for 99.98% purity Cu (Gubicza, Chinh, Lábár, Dobatkin, Hegedűs, &

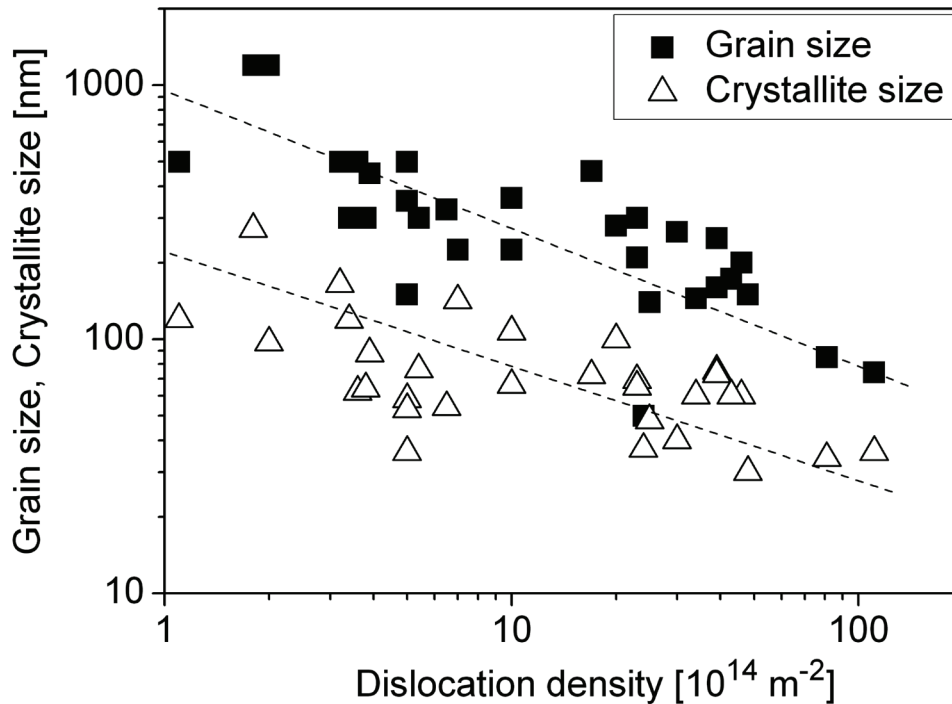
Figure 13. The dislocation density and the crystallite size as a function of the number ECAP passes for 99.98% purity Cu



Langdon, 2009), but the tendencies are similar for other metals. The dislocation density increases while the crystallite size decreases with increasing strain in ECAP up to 3 passes. The values obtained after 3 passes can be regarded as the saturation values achievable by ECAP in pure Cu at room temperature. The saturation of the dislocation density is a consequence of the dynamic equilibrium of the formation and annihilation of dislocations. The maximum dislocation density is reached usually after 2-4 passes of ECAP for the majority of metallic materials (Dalla Torre, Lapovok, Sandlin, Thomson, Davies, & Pereloma, 2004; Schafler, Steiner, Korznikova, Kerber, & Zehetbauer, 2005; Gubicza, Chinh, Krállics, Schiller, & Ungár, 2006). The grain size determined by TEM has similar evolution as for the crystallite size. The minimum grain and crystallite size values as a function of the maximum dislocation density obtained for different metals and alloys are plotted in Figure 14. The data are taken from Table 1. It can be concluded that, although there is no strict correlation between the grain or crystallite size and the dislocation density of the UFG metals processed by SPD procedures, the higher dislocation density is associated with smaller grain and crystallite sizes. This is a consequence of the fact that the basic mechanism of grain-refinement in SPD materials is the arrangement of dislocations into grain and subgrain boundaries.

The saturation dislocation density is determined by the dynamic equilibrium between the formation and annihilation of dislocations. The more difficult the dislocation annihilation during SPD-processing, the higher the maximum dislocation density. The annihilation processes are hindered by (i) the low homologous temperature of SPD, (ii) the solid solution alloying, (iii) the second phase particles and (iv) the high degree of dislocation dissociation due to the low stacking fault energy (SFE). The homologous temperature of SPD can be kept at low values either by processing at low temperatures or by applying SPD on metals having high melting points. Figure 15 illustrates that the higher the melting point (T_m)

Figure 14. The saturation grain and crystallite size values determined by TEM and X-ray line profile analysis, respectively, for SPD-processed UFG materials as a function of the saturation dislocation density. The data are plotted in double logarithmic scales as the values span about two orders of magnitude. The experimental error corresponds to the size of symbols.



in pure fcc metals having medium or high SFE (Al, Ni, Cu, and Au), the larger the maximum dislocation density achievable by ECAP at room temperature. It is noted that the maximum dislocation density increases while the minimum values of the crystallite and grain sizes decrease due to alloying. Figure 15 shows that the saturation dislocation density for pure Ag is much higher than the values for other fcc metals having similar melting points (Au, Cu). The very large dislocation density in Ag can be explained by its extremely low SFE, yielding a high degree of dislocation dissociation that hinders both cross-slip and climb thereby retarding dislocation annihilation.

The twin fault probability is plotted as a function of SFE for some fcc metals and alloys in Figure 16. It is revealed that the twin fault probability increases with decreasing SFE (Gubicza, 2012). At the same time, for same or similar SFE values, the smaller grain size is accompanied by larger twin boundary frequency. The higher probability of twinning is caused by the easier emission of twinning partials from grain boundaries with decreasing grain size.

The grain refinement in powder materials can be achieved by ball milling. It is noted that the crystallite size or the grain size in metallic powders processed by milling is usually smaller by 2-3 orders of magnitude than the powder particle size (Gubicza, 2012). This suggests that the final nanograins form rather inside the particles by similar mechanisms as in SPD of bulk metals than by the fracture of particles into nanosized fragments. Therefore, the milled particles usually remain large (their size may be even several microns), while the crystallite size can be reduced to several tens of nanometers. Despite

Practical Applications of X-Ray Line Profile Analysis

Table 1. The maximum dislocation density and the minimum crystallite size determined by X-ray line profile analysis, and the minimum grain size obtained by TEM for metallic materials processed by SPD. RT: room temperature, ECAP: equal-channel angular pressing, HPT: high-pressure torsion, MDF: multi-directional forging, TE: twist extrusion, CNT: carbon nanotube.

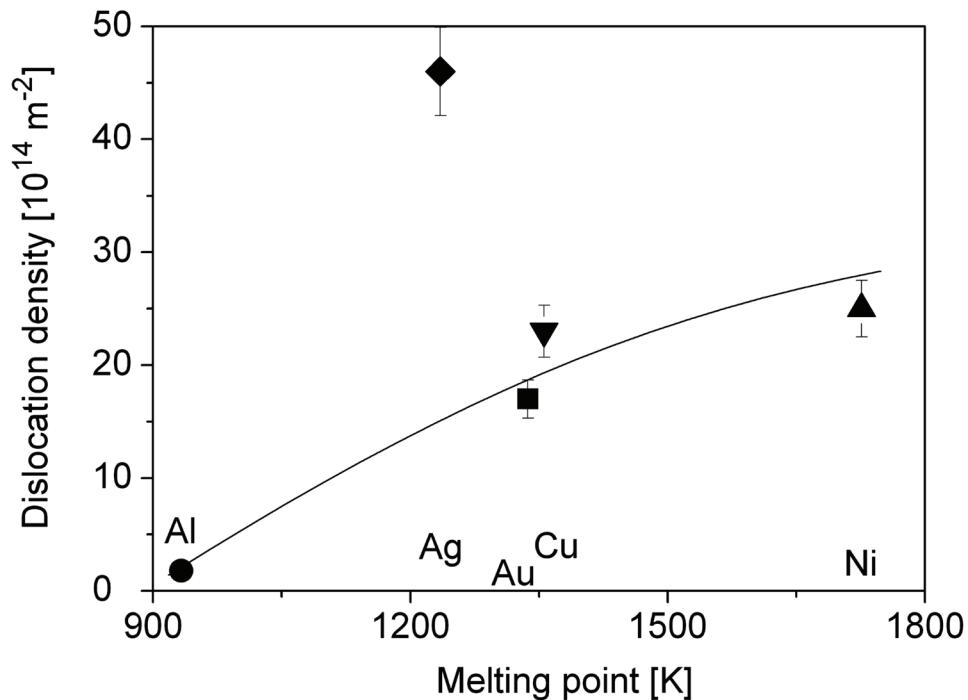
Material	Processing Method	Grain Size [nm]	Crystallite Size [nm]	Dislocation Density [10^{14} m^{-2}]	Reference
Pure Metals					
Al	ECAP at RT	1200	272	1.8	Gubicza, Chinh, Horita, and Langdon (2004)
Cu	ECAP at RT	210	69	23	Gubicza, Chinh, Lábár, Dobatkin, Hegedűs, and Langdon (2009)
Cu	HPT at RT	160	75	39	Gubicza, Dobatkin, Khosravi, Kuznetsov, and Lábár (2011)
Cu	MDF at RT	225	142	7	Gubicza, Dobatkin, Khosravi, Kuznetsov, and Lábár (2011)
Cu	TE at RT	225	107	10	Gubicza, Dobatkin, Khosravi, Kuznetsov, and Lábár (2011)
Au	ECAP at RT	460	72	17	Gubicza, Chinh, Szommer, Vinogradov, and Langdon (2007)
Ni	8 ECAP + 5 HPT at RT	140	48	25	Zhilyaev, Gubicza, Nurislamova, Révész, Surinach, Baró, and Ungár (2003)
Ag	ECAP at RT	200	60	46	Gubicza, Chinh, Lábár, Hegedűs, and Langdon (2010)
Ti	ECAP at 700 K	265	40	30	Zhu, Huang, Gubicza, Ungár, Wang, Ma, and Valiev (2003)
Solid Solution Alloys					
Al-1%Mg	ECAP at RT	450	88	3.9	Gubicza, Chinh, Krállics, Schiller, and Ungár (2006)
Al-3%Mg	ECAP at RT	300	65	23	Gubicza, Chinh, Krállics, Schiller, and Ungár (2006)
IF Steel	ECAP at RT	360	66	10	Máthis, Krajnák, Kuzel, and Gubicza (2011)
Cu-10%Zn	HPT at RT	145	60	34	Balogh, Ungár, Zhao, Zhu, Horita, Xu, and Langdon (2008)
Cu-30%Zn	HPT at RT	85	34	81	Balogh, Ungár, Zhao, Zhu, Horita, Xu, and Langdon (2008)
Dispersion-Strengthened Alloys					
Al 6082	ECAP at RT	300	76	5.4	Gubicza, Chinh, Krállics, Schiller, and Ungár (2006)
Al-4.8%Zn-1.2%Mg-0.14%Zr	ECAP at 473 K	500	165	3.2	Gubicza, Schiller, Chinh, Illy, Horita, and Langdon (2007)
Al-5.7%Zn-1.9%Mg-0.35%Cu	ECAP at 473 K	300	119	3.4	Gubicza, Schiller, Chinh, Illy, Horita, and Langdon (2007)
Al-5.9%Mg-0.3%Sc-0.18%Zr	HPT at RT	50	37	24	Fátay, Bastarash, Nyilas, Dobatkin, Gubicza, and Ungár (2003)
Mg-9%Al-1%Zn-0.2%Mn	ECAP at 543 K	1200	97	2.0	Máthis, Gubicza, and Nam (2005)
Mg-3%Al-1%Zn	ECAP at 553 K	500	120	1.1	Janecek, Cízek, Gubicza, and Vrátná (2012)

continued on following page

Table 1. Continued

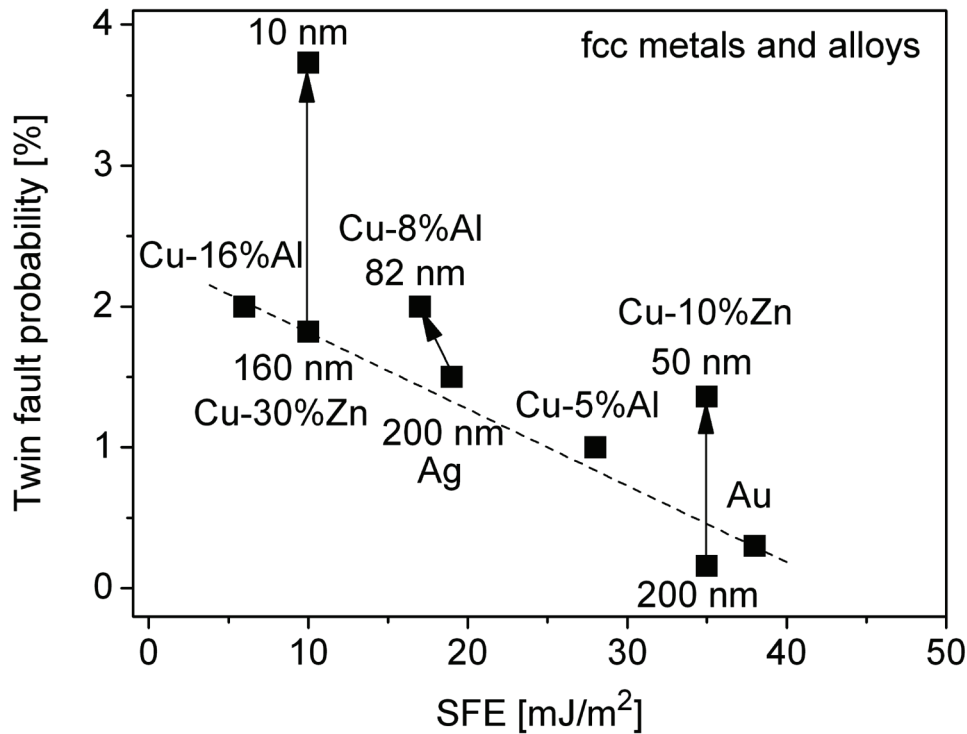
Material	Processing Method	Grain Size [nm]	Crystallite Size [nm]	Dislocation Density [10^{14} m^{-2}]	Reference
Mg-4.3%Zn-0.7%Y	HPT at RT	350	58	5	Jenei, Gubicza, Yoon, and Kim (2012)
Mg-4.3%Zn-0.7%Y	HPT at 373 K	500	62	3.6	Jenei, Gubicza, Yoon, and Kim (2012)
Cu-5%Ag	Rolling at 77 K	150	30	48	Sitarama Raju, Subramanya Sarma, Kauffmann, Hegedús, Gubicza, Peterlechner, Freudenberger, and Wilde (2013)
Cu-0.18%Zr	HPT at RT	280	100	20	Dopita, Janecek, Kuzel, Seifert, and Dobatkin (2010)
Cu-0.18%Zr	ECAP at RT	250	73	39	Kuzel, Janecek, Matej, Cizek, Dopita, and Srba (2010)
Cu-3%CNT	HPT at RT	74	36	111	Jenei, Yoon, Gubicza, Kim, Lábár, and Ungár (2011)

Figure 15. The saturation crystallite size and dislocation density as a function of melting point for different pure fcc metals processed by ECAP at room temperature



the similar grain refinement mechanisms as in SPD-processing of bulk materials, milling results in much higher maximum dislocation density and smaller crystallite size. These deviations can be explained by the retarding effect of the impurities introduced into the powder during milling and the high pressure induced by the collision between powder particles and balls. Under special conditions the dislocation density may become extremely high. For instance, in high purity iron powder milled for one week the

Figure 16. The twin fault probability as a function of SFE for fcc metals and alloys processed by SPD. The grain size is also given at some datum points. The arrows indicate the increase of twin fault probability with decreasing grain size. Data taken from Gubicza (2012).



dislocation density increased up to $165 \times 10^{14} \text{ m}^{-2}$ while the crystallite size was refined down to 10-20 nm (Révész, Ungár, Borbély, & Lendvai, 1996). For alloys the maximum dislocation density is even larger. In the case of ball milled $\text{Fe}_{50}\text{Co}_{50}$ (wt. %), $\text{Fe}_{80}\text{Cu}_{20}$ (at. %) and $\text{Fe}_{92}\text{Al}_2\text{Si}_6$ (wt. %) powders the crystallites with the average size of ~ 10 nm contained very large dislocation density of $4000\text{-}5000 \times 10^{14} \text{ m}^{-2}$ (Shen, Schwarz, & Thompson, 2005; Moumenia, Nemamcha, Alleg, & Greneche, 2010). It was also revealed that the edge character of dislocations in both metals (Gubicza, 2012) and ceramics (Sen, Das, & Das 2011) becomes stronger with increasing milling time as determined from the dislocation contrast factors obtained by X-ray line profile analysis. This effect can be explained by the much easier annihilation of screw dislocations by cross-slip than edge dislocations by climb during severe deformation in the milling process.

Very high values of the dislocation density in nanomaterials can be achieved even without the application of SPD or milling methods (Gubicza, 2012). For instance, in a Cu nanopowder produced by inert-gas condensation, the dislocation density was found to be $47 \times 10^{14} \text{ m}^{-2}$ (Ungár, Ott, Sanders, Borbély, & Weertman, 1998) which is close to the value obtained in Cu by HPT (see Table 1). However, these dislocations are most probably related to the particle growth mechanism as they have screw character as determined by X-ray line profile analysis while the dislocations form during SPD usually have rather edge character. The crystallite size determined by X-ray line profile analysis was ~ 21 nm which agrees well with the grain size obtained by TEM (~ 16 nm), revealing the lack of subgrain structure inside grains (Gubicza, 2012). The average distance between dislocation is 15 nm as calculated from

the inverse square-root of the dislocation density. Comparing this value with the grain size, it is suggested that a grain contains about two dislocations in average. Therefore, the relatively high dislocation density in inert-gas condensed Cu powder is caused only by the small grain size and not by the large number of dislocations inside the individual grains (Gubicza, 2012). Additionally, a significant value of twin boundary frequency, 3.6%, is detected by X-ray line profile analysis which agrees well with the value determined by TEM (3.4%). High dislocation densities of $\sim 120 \times 10^{14} \text{ m}^{-2}$ and $\sim 30 \times 10^{14} \text{ m}^{-2}$ were also found in nanocrystalline CeO_2 powders with the crystallite sizes of ~ 4 and ~ 18 nm, respectively, processed by calcination of grounded ceria xerogel at 300 and 600 °C (Scardi, Leoni, Müller, & Di Maggio, 2010). In these powders the average number of dislocations per crystallite was ~ 1 or even smaller. Furthermore, in lead sulphide (PbS) nanocrystals with the crystallite size of ~ 15 nm synthesized by a chemical method the dislocation density had extremely large values of $\sim 3000 \times 10^{14} \text{ m}^{-2}$ (Kalita, Deka, Das, Hazarika, Dey, Das, Paul, Sarmah, & Sarma, 2012).

Dense UFG and nanocrystalline ceramics are usually produced by sintering of powders. The effect of the size distribution of the starting ceramic powders and the sintering conditions (e.g. temperature and pressure) on the microstructure of the compacted bulk material has been studied by X-ray line profile analysis in several papers (Balzar, Audebrand, Daymond, Fitch, Hewat, Langford, Le Bail, Louër, Masson, McCowan, Popa, Stephens, & Toby, 2004; Gubicza & Ungár, 2007; Louer, Auffredic, Langford, Ciosmak, & Niepce, 1983; Ungár, Borbély, Goren-Muginstein, Berger, & Rosen, 1999). Louer, Auffredic, Langford, Ciosmak, and Niepce (1983) have determined the shape, size and size distribution of crystallites in nanocrystalline ZnO powder synthesized by thermal decomposition of zinc hydroxinitrate. Although the line breadths showed a strong *hkl* dependence, the harmonic pairs of reflections, e.g. *100-300* and *002-004* were identical within experimental errors. These observations were attributed to the shape anisotropy of the crystallites. In the quantitative evaluation of the Fourier transforms of the profiles, the crystallites are modeled by cylinders. It was found that the axis of the cylinder was parallel to the hexagonal *c* axis and the average diameter and height were 11 and 24 nm, respectively. TEM micrographs have confirmed the same shape anisotropy and average size values, although they showed that the real shape of the crystallites is prism with irregular hexagonal cross section. X-ray line profile analysis was also performed on bulk UFG tungsten-carbide specimen produced by ball-milling of sub-micron size powder and subsequent sintering at 1420 °C (Ungár, Borbély, Goren-Muginstein, Berger, & Rosen, 1999). The line breadths decreased down to about one-third during sintering as a consequence of the grain-growth at high temperature consolidation. There was a good agreement between the crystallite size distribution determined by line profile analysis and the grain size distribution obtained by TEM. A similar observation was made by Balzar, Audebrand, Daymond, Fitch, Hewat, Langford, Le Bail, Louer, Masson, McCowan, Popa, Stephens, and Toby (2004) on CeO_2 ceramic powder with the mean crystallite size of about 3 nm. This powder was prepared by decomposition of $\text{Ce}_2\text{O}(\text{NO}_3)_6 \cdot \text{H}_2\text{O}$ in nitrogen atmosphere at 230 °C. The strain contribution to peak broadening in this material was negligible.

The influence of sintering pressure and temperature on the defect structure in low SFE ceramics was illustrated with the experiments performed on SiC consolidated from a nanopowder with the particle size of 30 nm (Gubicza, Nauyoks, Balogh, Lábár, Zerda, & Ungár, 2007). The sintering procedure was carried out at temperatures of 1400, 1600 and 1800 °C. At each temperature, specimens were sintered at pressures of 2, 4 and 5.5 GPa. X-ray line profile analysis revealed that in the initial powder the twin fault probability was very high (7.4%), while the dislocation density was below the limit of detection by X-ray line broadening, i.e. smaller than 10^{13} m^{-2} . From the results it can be concluded that in the initial SiC nanopowder the main lattice defects were twin boundaries, most probably due to the extremely low

SFE of SiC (0.2 mJ/m^2 (Ning & Pirouz, 1996)). During sintering at low pressures and temperatures, the twin fault probability increased to 11% and the dislocation density remained below the detection limit of line profile analysis. At 1600 °C and 1800 °C, and above a certain pressure limit, the twin fault probability decreased to a very low value of 0.1%, and dislocations became the main type of lattice defects with a density of about $4 \times 10^{14} \text{ m}^{-2}$. The values of the pressure limit were 5.5 and 4 GPa at 1600 °C and 1800 °C, respectively, i.e. this limit decreased with increasing temperature (Gubicza, Nauyoks, Balogh, Lábár, Zerda, & Ungár, 2007).

Bulk nanostructured diamond may be consolidated from nanopowders under high pressure and high temperature conditions. From the agreement between the particle size distributions of the starting powders obtained by line profile analysis and BET method, it was concluded that the diamond particles were single crystals similarly as for ceramic powders (Palosz, Grzanka, Pantea, Zerda, Gubicza, & Ungár, 2005). The Williamson-Hall plots showed that the particles with the size smaller than 30 nm were dislocation free but they contained significant amount of planar faults. The diamond powders with the particle size higher than 30 nm contained dislocations and their density increased during sintering procedure. Bulk UFG diamond can also be processed by sintering of micron-sized powders. During consolidation at high pressures and temperatures, dislocations were formed and the grains were divided into subgrains or dislocation cells, similarly as in metals processed by severe plastic deformation (Palosz, Grzanka, Pantea, Zerda, Gubicza, & Ungár, 2005). The dislocation formation was induced by the contact shear stresses exerted by the edges of neighboring particles in the compressed powder.

APPLICATION OF X-RAY LINE PROFILE ANALYSIS ON POLYMERS

Diffraction peak profile analysis has also been applied to study the defects in crystalline polymers (Hofmann & Walenta, 1987; Schafler & Zehetbauer, 2005; Spieckermann, Wilhelm, Kerber, Schafler, Polt, Bernstorff, Addiego, & Zehetbauer, 2010; Wilhelm, Paris, Schafler, Bernstorff, Bonarski, Ungár, & Zehetbauer, 2004). The crystallite size obtained for isostatic polypropylene (iPP) by X-ray line profile analysis was in good correlation with the lamella thickness (Wilhelm, Paris, Schafler, Bernstorff, Bonarski, Ungár, & Zehetbauer, 2004). A comparison of the crystallite size distribution with the lamellae size distribution determined by DSC yielded an excellent agreement (Spieckermann, Wilhelm, Kerber, Schafler, Polt, Bernstorff, Addiego, & Zehetbauer, 2010; Kerber, Zehetbauer, Schafler, Spieckermann, Bernstorff, & Ungár, 2011). The determination of size distributions from DSC is based on the fact that the melting temperature is related to the thickness of the plate-like crystallites. The evolution of the crystallite size and the lattice defect structure in iPP during plastic deformation has also been studied. It was found that in monoclinic α -phase iPP the crystallite size decreased from 20 nm to 15 nm due to rolling up to the true strain of 50% (Wilhelm, Paris, Schafler, Bernstorff, Bonarski, Ungár, & Zehetbauer, 2004). The Williamson-Hall plot revealed a strong order dependence of peak breadths. Using the average dislocation contrast factors, the FWHM values can be arranged along a smooth curve in the modified Williamson-Hall plot (see Chapter 6). This means that the lattice defects in melt-crystallized and plastically deformed polypropylene have the same type of strain field as for dislocations, therefore we can handle these defects as dislocations. The dislocation density was evaluated by CMWP fitting method. It was found that the dislocation density increased with deformation. The dislocation densities in the initial and the plastically deformed iPP were 10^{14} - 10^{15} m^{-2} and 10^{16} - 10^{17} m^{-2} , respectively (Spieckermann, Wilhelm, Kerber, Schafler, Polt, Bernstorff, Addiego, & Zehetbauer, 2010; Wilhelm,

Paris, Schafler, Bernstorff, Bonarski, Ungár, & Zehetbauer, 2004). The latter values are 1-2 orders of magnitude higher than the values in deformed metals. This can be explained by the long-chain nature of the macromolecules in iPP which results in additional constraints when polymer crystals develop. This leads to a strong production of dislocations already in the undeformed materials. The higher initial dislocation density might yield higher number of sources for dislocation generation during deformation compared to metallic materials.

CONCLUSION

The instrumental broadening of diffraction peaks should be taken into account in line profile analysis. The instrumental peak profiles for a given diffraction setting can be measured on a standard material which has large crystals with small concentration of lattice defects. The instrumental correction can be carried out by the Stokes-method in which the Fourier transform of the physical profile is obtained as the ratio of the Fourier transforms of the experimental and instrumental profiles. The uncertainty of this calculation is relatively high for large values of the Fourier variable where nearly zero values of the Fourier transforms are divided by each other or when the instrumental broadening is very close to the experimental one. In the latter case the experimental profile is suggested to fit by the convolution of the closest instrumental peak and an assumed physical profile. This refinement procedure can yield a reliable physical peak profile. Since the addition rule of widths of convoluted peaks depends strongly on the shape of profiles, the application of any relationship for instrumental correction of peak breadth is very uncertain.

In hexagonal crystals each of the eleven dislocation slip systems has different contrast effect on peak broadening, therefore the comparison of the experimental contrast factors with the theoretical values calculated for the different slip systems enables the determination of the prevailing dislocation slip systems in the specimen. Two procedures referred to as *Hexburger* and *b2C* were elaborated for the determination of the fractions of the various slip systems. The fundamental difference between methods *Hexburger* and *b2C* is that in the former procedure the fractions of slip systems in the various Burgers vector groups may be different while in the latter one the non-zero fractions for all Burgers vector groups are equal. The determination of the fractions of $\langle a \rangle$ and $\langle c+a \rangle$ dislocations is facilitated by the opposite signs of the broadening effects of $\langle a \rangle$ and $\langle c+a \rangle$ edge dislocations on many reflections. This means that for a given reflection $\langle a \rangle$ and $\langle c+a \rangle$ edge dislocations cause broader and narrower breadths, respectively, relative to the width of reflections $hk0$. The application of these procedures revealed the abundance of $\langle a \rangle$ -type dislocations besides the $\langle c \rangle$ - and $\langle c+a \rangle$ -type dislocations which can be explained by the lowest formation energy of the former dislocation type. The plastic deformation at elevated temperatures yielded an increase of the fraction of $\langle c+a \rangle$ -type dislocations due to the reduction of their critical resolved shear stress with increasing temperature.

For plastically deformed metallic materials the crystallite size determined by X-ray line profile analysis is usually much smaller than the grain or particle size obtained by TEM or SEM, respectively. This phenomenon can be attributed to the fact that the crystallites are equivalent to the domains in the microstructure which scatter X-rays coherently. As the coherency of X-rays breaks even if they are scattered from volumes having quite small misorientation, the crystallite size corresponds rather to the subgrain size in the severely deformed microstructures. Besides low angle grain boundaries, dipolar dislocation walls resulting in zero misorientation between the separated regions (cells) can also break down

coherency of X-ray scattering. In this case, the crystallite size is equivalent to the size of cells between the walls. However, in the case of periodically distributed low-angle grain boundaries the crystallite size determined by the Warren-Averbach procedure is larger than the spacing between the boundaries by a factor of about two when the spacing between the boundaries is close to the spacing between the dislocations within the boundaries. This phenomenon is associated with the negative curvature on the size Fourier transform for small values of Fourier variable, which is called “hook” effect. For metallic and ceramic materials processed in either bulk or powder form without the application of severe plastic deformation the crystallite size obtained by X-ray line profile analysis agrees well with the grain or particle size determined by TEM due to the lack of subgrain structure. In general, diffraction peak profile analysis and TEM give complementary information about the microstructure. For instance, X-ray line profile analysis and TEM usually can be applied successfully for large and low defect densities, respectively, although these regimes usually overlap. The detection limits of X-ray peak profile analysis for the crystallite size, dislocation density and twin fault probability are 400-800 nm (upper limit), 10^{12} - 10^{13} m⁻² (lower limit) and 0.02-0.1% (lower limit), respectively. The vacancy concentration can be estimated by the combination of line profile analysis and residual electrical resistometry or differential scanning calorimetry. Vacancies have a considerable contribution to the diffuse background scattering under X-ray diffraction peaks, therefore the ratio of the integrated background and the integrated peak intensities can be used for the determination of vacancy concentration after a calibration procedure.

The application of X-ray line profile analysis on severely deformed metallic materials shows that the dislocation density increases while the crystallite size decreases with increasing strain and saturation is reached at a strain of 2-4. The saturation dislocation density and crystallite size at room temperature are larger and smaller, respectively, for higher melting point, lower SFE and larger alloying concentration. The twin fault probability in fcc metallic and ceramic materials increases with decreasing SFE and grain size. In polymers the crystallite size obtained by X-ray line profile analysis is in good correlation with the lamella thickness. The Williamson-Hall plot of peak breadths revealed that lattice defects in polymers have the same type of strain field as for dislocations, therefore we can handle these defects as dislocations. The dislocation densities in the as-processed and the plastically deformed polymers are 1-2 orders of magnitude higher than the values in metals.

REFERENCES

- Balogh, L., Tichy, G., & Ungár, T. (2009). Twinning on pyramidal planes in hexagonal close packed crystals determined along with other defects by X-ray line profile analysis. *Journal of Applied Crystallography*, *42*, 580–591.
- Balogh, L., Ungár, T., Zhao, Y., Zhu, Y. T., Horita, Z., Xu, C., & Langdon, T. G. (2008). Influence of stacking-fault energy on microstructural characteristics of ultrafine-grain copper and copper-zinc alloys. *Acta Materialia*, *56*, 809–820.
- Balzar, D., Audebrand, N., Daymond, M. R., Fitch, A., Hewat, A., & Langford, J. I. et al. (2004). Size-strain line-broadening analysis of the ceria round-robin sample. *Journal of Applied Crystallography*, *37*, 911–924.

Cernansky, M. (2000). Extrapolation method of the elimination of instrumental broadening of diffraction lines. *Materials and Structures*, 7, 3–5.

Cheary, R. W., & Cline, J. P. (1994). Instrumental conditions on the shapes of x-ray powder line profiles. *Advances in X-Ray Analysis*, 38, 75–82.

Cheary, R. W., & Coelho, A. (1992). A fundamental parameters approach to x-ray line-profile fitting. *Journal of Applied Crystallography*, 25, 109–121.

Chun, Y. B., Yu, S. H., Semiatin, S. L., & Hwang, S. K. (2005). Effect of deformation twinning on microstructure and texture evolution during cold rolling of CP-titanium. *Materials Science and Engineering A*, 398, 209–219.

Cizek, J., Janecek, M., Srba, O., Kuzel, R., Barnovska, Z., Prochazka, I., & Dobatkin, S. (2011). Evolution of defects in copper deformed by high-pressure torsion. *Acta Materialia*, 59, 2322–2329.

Dalla Torre, F., Lapovok, R., Sandlin, J., Thomson, P. F., Davies, C. H. J., & Pereloma, E. V. (2004). Microstructures and properties of copper processed by equal channel angular extrusion for 1–16 passes. *Acta Materialia*, 52, 4819–4832.

Dopita, M., Janecek, M., Kuzel, R., Seifert, H. J., & Dobatkin, S. (2010). Microstructure evolution of CuZr polycrystals processed by high-pressure torsion. *Journal of Materials Science*, 45, 4631–4644.

Dragomir, I. C., & Ungár, T. (2002). Contrast factors of dislocations in the hexagonal crystal system. *Journal of Applied Crystallography*, 35, 556–564.

Eckstein, H. (1945). Disorder scattering of x-rays by local distortions. *Physical Review*, 68, 120–124.

Fátay, D., Bastarash, E., Nyilas, K., Dobatkin, S., Gubicza, J., & Ungár, T. (2003). X-ray diffraction study on the microstructure of an Al–Mg–Sc–Zr alloy deformed by high-pressure torsion. *Zeitschrift für Metallkunde*, 94, 842–847.

Gozzo, F., Cervellino, A., Leoni, M., Scardi, P., Bergamaschi, A., & Schmitt, B. (2010). Instrumental profile of MYTHEN detector in Debye-Scherrer geometry. *Zeitschrift für Kristallographie*, 225, 616–624.

Gubicza, J. (2012). *Defect structure in nanomaterials*. Cambridge, UK: Woodhead Publishing Ltd.

Gubicza, J., & Chinh, N. Q., Krállics, Gy., Schiller, I., & Ungár, T. (2006). Microstructure of ultrafine-grained fcc metals produced by severe plastic deformation. *Current Applied Physics*, 6, 194–199.

Gubicza, J., Chinh, N. Q., Horita, Z., & Langdon, T. G. (2004). Effect of Mg addition on microstructure and mechanical properties of aluminum. *Materials Science and Engineering A*, 387–389, 55–59.

Gubicza, J., Chinh, N. Q., Lábár, J. L., Dobatkin, S., Hegedűs, Z., & Langdon, T. G. (2009). Correlation between microstructure and mechanical properties of severely deformed metals. *Journal of Alloys and Compounds*, 483, 271–274.

Gubicza, J., Chinh, N. Q., Lábár, J. L., Hegedűs, Z., & Langdon, T. G. (2010). Principles of self-annealing in silver processed by equal-channel angular pressing: The significance of a very low stacking fault energy. *Materials Science and Engineering A*, 527, 752–760.

Practical Applications of X-Ray Line Profile Analysis

Gubicza, J., Chinh, N. Q., Szommer, P., Vinogradov, A., & Langdon, T. G. (2007). Microstructural characteristics of pure gold processed by equal-channel angular pressing. *Scripta Materialia*, 56, 947–950.

Gubicza, J., Dobatkin, S. V., Khosravi, E., Kuznetsov, A. A., & Lábár, L. J. (2011). Microstructural stability of Cu processed by different routes of severe plastic deformation. *Materials Science and Engineering A*, 528, 1828–1832.

Gubicza, J., Dragomir, I. C., Ribárik, G., Baik, S. C., Zhu, Y. T., Valiev, R. Z., & Ungár, T. (2003). Dislocation structure and crystallite size-distribution in plastically deformed Ti determined by x-ray peak profile analysis. *Zeitschrift fur Metallkunde*, 94, 1185–1188.

Gubicza, J., Dragomir, I. C., Ribárik, G., Zhu, Y. T., Valiev, R. Z., & Ungár, T. (2003). Microstructure of severely deformed titanium from x-ray diffraction profile analysis. *Materials Science Forum*, 414-415, 229–234.

Gubicza, J., Nam, N. H., Balogh, L., Hellmig, R. J., Stolyarov, V. V., Estrin, Y., & Ungár, T. (2004). Microstructure of severely deformed metals determined by x-ray peak profile analysis. *Journal of Alloys and Compounds*, 378, 248–252.

Gubicza, J., Nauyoks, S., Balogh, L., Lábár, J., Zerda, T. W., & Ungár, T. (2007). Influence of sintering temperature and pressure on crystallite size and lattice defect structure in nanocrystalline SiC. *Journal of Materials Research*, 22, 1314–1321.

Gubicza, J., Ribárik, G., Goren-Muginstein, G. R., Rosen, A. R., & Ungár, T. (2001). The density and the character of dislocations in cubic and hexagonal polycrystals determined by x-ray diffraction. *Materials Science and Engineering A*, 309-310, 60–63.

Gubicza, J., Schiller, I., Chinh, N. Q., Illy, J., Horita, Z., & Langdon, T. G. (2007). The effect of severe plastic deformation on precipitation in supersaturated Al-Zn-Mg alloys. *Materials Science and Engineering A*, 460-461, 77–85.

Gubicza, J., Szépvölgyi, J., Mohai, I., Zsoldos, L., & Ungár, T. (2000). Particle size distribution and the dislocation density determined by high resolution x-ray diffraction in nanocrystalline silicon nitride powders. *Materials Science and Engineering A*, 280, 263–269.

Gubicza, J., & Ungár, T. (2007). Characterization of defect structures in nanocrystalline materials by x-ray line profile analysis. *Zeitschrift fur Kristallographie*, 222, 567–579.

Hofmann, D., & Walenta, E. (1987). An improved single-line method for the wide-angle x-ray scattering profile analysis of polymers. *Polymer*, 28, 1271–1276.

Huang, K. (1947). X-ray reflexions from dilute solid solutions. *Proceedings - Royal Society. Mathematical, Physical and Engineering Sciences*, 190, 102–117. PMID:20255303

Humphreys, F. J., & Hatherly, M. (2004). *Recrystallization and related annealing phenomena*. Oxford, UK: Elsevier.

Janecek, M., Cízek, J., Gubicza, J., & Vrátná, J. (2012). Microstructure and defect structure evolution in MgAlZn alloy processed by severe plastic deformation. *Journal of Materials Science*, 47, 7860–7869.

- Jenei, P., Gubicza, J., Yoon, E. Y., & Kim, H. S. (2012). X-ray diffraction study on the microstructure of a Mg-Zn-Y alloy consolidated by high-pressure torsion. *Journal of Alloys and Compounds*, *539*, 32–35.
- Jenei, P., Yoon, E. Y., Gubicza, J., Kim, H. S., Lábár, J. L., & Ungár, T. (2011). Microstructure and hardness of copper - carbon nanotube composites consolidated by high pressure torsion. *Materials Science and Engineering A*, *528*, 4690–4695.
- Kalita, M. P. C., Deka, K., Das, J., Hazarika, N., Dey, P., & Das, R. et al. (2012). X-ray diffraction line profile analysis of chemically synthesized lead sulphide nanocrystals. *Materials Letters*, *87*, 84–86.
- Kerber, M. B., Zehetbauer, M. J., Schafner, E., Spieckermann, F. C., Bernstorff, S., & Ungár, T. (2011). X-ray line profile analysis—An ideal tool to quantify structural parameters of nanomaterials. *JOM*, *63*, 61–84.
- Klug, H. P., & Alexander, L. E. (1974). *X-ray diffraction procedures for polycrystalline and amorphous materials*. New York: John Wiley and Sons.
- Krivoglaz, M. A. (1969). *Theory of x-ray and thermal neutron scattering by real crystals*. New York: Plenum Press.
- Kuzel, R., Janecek, M., Matej, Z., Cizek, J., Dopita, M., & Srba, O. (2010). Microstructure of equal-channel angular pressed Cu and Cu-Zr samples studied by different methods. *Metallurgical and Materials Transactions A*, *41*, 1174-1190.
- Kuzel, R. Jr, & Klimanek, P. (1988). X-ray diffraction line broadening due to dislocations in non-cubic materials: The case of elastic anisotropy applied to hexagonal crystals. *Journal of Applied Crystallography*, *21*, 363–368.
- Langford, J. I. (1968). The variance and other measures of line broadening in powder diffractometry: Practical consideration. *Journal of Applied Crystallography*, *1*, 48–59.
- Langford, J. I., Cernik, R. J., & Louer, D. (1991). The breadth and shape of instrumental line profiles in high-resolution powder diffraction. *Journal of Applied Crystallography*, *24*, 913–919.
- Langford, J. I., & Louer, D. (1996). Powder diffraction. *Reports on Progress in Physics*, *59*, 131–234.
- Leoni, M., Scardi, P., & Langford, J. I. (1998). Characterization of standard reference materials for obtaining instrumental line profiles. *Powder Diffraction*, *13*, 210–215.
- Leoni, M., Welzel, U., & Scardi, P. (2004). Polycapillary optics for materials science studies: Instrumental effects and their correction. *Journal of Research of the National Institute of Standards and Technology*, *109*, 27–48.
- Lin, J. D., & Duh, J. G. (1997). The use of X-ray line profile analysis in the tetragonal to monoclinic phase transformation of ball milled, as-sintered and thermally aged zirconia powders. *Journal of Materials Science*, *32*, 4901–4908.
- Louer, D., Auffredic, J. P., Langford, J. I., Ciosmak, D., & Niepce, J. C. (1983). A precise determination of the shape, size and distribution of size of crystallites in zinc oxide by x-ray line-broadening analysis. *Journal of Applied Crystallography*, *16*, 183–191.

Practical Applications of X-Ray Line Profile Analysis

Louer, D., & Langford, J. I. (1988). Peak shape and resolution in conventional diffractometry with monochromatic X-rays. *Journal of Applied Crystallography*, *21*, 430–437.

Máthis, K., Gubicza, J., & Nam, N. H. (2005). Microstructure and mechanical behavior of AZ91 Mg-alloy processed by equal channel angular pressing. *Journal of Alloys and Compounds*, *394*, 194–199.

Máthis, K., Krajnák, T., Kuzel, R., & Gubicza, J. (2011). Structure and mechanical behaviour of interstitial-free steel processed by equal-channel angular pressing. *Journal of Alloys and Compounds*, *509*, 3522–3525.

Máthis, K., Nyilas, K., Axt, A., Dragomir, I. C., Ungár, T., & Lukác, P. (2004). The evolution of non-basal dislocations as a function of deformation temperature in pure magnesium determined by x-ray diffraction. *Acta Materialia*, *52*, 2889–2894.

Mingler, B., Stolyarov, V. V., Zehetbauer, M., Lacom, W., & Karnthaler, H. P. (2006). TEM investigations of titanium processed by ECAP followed by cold rolling. *Materials Science Forum*, *503-504*, 805–810.

Moumenia, H., Nemamcha, A., Alleg, S., & Greneche, J. M. (2010). Stacking faults and structure analysis of ball-milled Fe–50%Co powders. *Materials Chemistry and Physics*, *122*, 439–443.

Ning, X. J., & Pirouz, P. (1996). A large angle convergent beam electron diffraction study of the core nature of dislocations in 3C-SiC. *Journal of Materials Research*, *11*, 884–894.

Palosz, B., Grzanka, E., Pantea, C., Zerda, T. W., Gubicza, J., & Ungár, T. (2005). Microstructure of nanocrystalline diamond powders studied by powder diffractometry. *Journal of Applied Physics*, *97*, 064316.

Paton, N. E., & Backofen, W. A. (1970). Plastic deformation of titanium at elevated temperatures. *Metalurgical Transactions A*, *1*, 2839–2847.

Rachinger, W. A. (1948). A correction for the $\alpha_1\alpha_2$ doublet in the measurement of widths of x-ray diffraction lines. *Journal of Scientific Instruments*, *25*, 254–255.

Révész, Á., Ungár, T., Borbély, A., & Lendvai, J. (1996). Dislocations and grain size in ball-milled iron powder. *Nanostructured Materials*, *7*, 779–788.

Samadi Khoshkhou, M., Scudino, S., Thomas, J., Gemming, T., Wendrock, H., & Eckert, J. (2013). Size evaluation of nanostructured materials. *Materials Letters*, *108*, 343–345.

Scardi, P., Leoni, M., Cappuccio, G., Langford, J. I., & Cernik, R. J. (1996). The breadth and shape of instrumental line profiles for the powder diffraction station 2.3 at the daresbury laboratory SRS. *Materials Science Forum*, *228-231*, 207–212.

Scardi, P., Leoni, M., Müller, M., & Di Maggio, R. (2010). In situ size-strain analysis of nanocrystalline ceria growth. *Materials Science and Engineering A*, *528*, 77–82.

Scardi, P., Lutterotti, L., & Maistrelli, P. (1994). Experimental determination of the instrumental broadening in the Bragg-Brentano geometry. *Powder Diffraction*, *9*, 180–186.

- Schafler, E., Simon, K., Bernstorff, S., Hanák, P., Tichy, G., Ungár, T., & Zehetbauer, M. J. (2005). A second-order phase-transformation of the dislocation structure during plastic deformation determined by in situ synchrotron x-ray diffraction. *Acta Materialia*, *53*, 315–322.
- Schafler, E., Steiner, G., Korznikova, E., Kerber, M., & Zehetbauer, M. J. (2005). Lattice defect investigation of ECAP-Cu by means of x-ray line profile analysis, calorimetry and electrical resistometry. *Materials Science and Engineering A*, *410-411*, 169–173.
- Schafler, E., & Zehetbauer, M. (2005). Characterization of nanostructured materials by x-ray line profile analysis. *Review on Advanced Materials Science*, *10*, 28–33.
- Sen, R., Das, S., & Das, K. (2011). Microstructural characterization of nanosized ceria powders by x-ray diffraction analysis. *Metallurgical and Materials Transaction A*, *42*, 1409-1417.
- Shen, T. D., Schwarz, R. B., & Thompson, J. D. (2005). Soft magnetism in mechanically alloyed nanocrystalline materials. *Physical Review B: Condensed Matter and Materials Physics*, *72*, 014431.
- Sitarama Raju, K., Subramanya Sarma, V., Kauffmann, A., Hegedűs, Z., Gubicza, J., & Peterlechner, M. et al. (2013). High strength and ductile ultrafine grained Cu-Ag alloy through bimodal grain size, dislocation density and solute distribution. *Acta Materialia*, *61*, 228–238.
- Spieckermann, F., Wilhelm, H., Kerber, M., Schafler, E., Polt, G., & Bernstorff, S. et al. (2010). Determination of lamella thickness distributions in isotactic polypropylene by x-ray line profile analysis. *Polymer*, *51*, 4195–4199.
- Trinkaus, H. (1972). On determination of the double-force tensor of point defects in cubic crystals by diffuse x-ray scattering.[b]. *Physica Status Solidi*, *51*, 307–319.
- Ungár, T., Borbély, A., Goren-Muginstein, G. R., Berger, S., & Rosen, A. R. (1999). Particle-size, size distribution and dislocations in nanocrystalline tungsten-carbide. *Nanostructured Materials*, *11*, 103–113.
- Ungár, T., Castelnau, O., Ribárik, G., Drakopoulos, M., Bechade, J. L., & Chauveau, T. et al. (2007). Grain to grain slip activity in plastically deformed Zr determined by X-ray micro-diffraction line profile analysis. *Acta Materialia*, *55*, 1117–1127.
- Ungár, T., Glavicic, M. G., Balogh, L., Nyilas, K., Salem, A. A., Ribárik, G., & Semiatin, S. L. (2008). The use of x-ray diffraction to determine slip and twinning activity in commercial-purity (CP) titanium. *Materials Science and Engineering A*, *493*, 79–85.
- Ungár, T., Gubicza, J., Ribárik, G., & Borbély, A. (2001). Crystallite size-distribution and dislocation structure determined by diffraction profile analysis: Principles and practical application to cubic and hexagonal crystals. *Journal of Applied Crystallography*, *34*, 298–310.
- Ungár, T., Ott, S., Sanders, P., Borbély, A., & Weertman, J. R. (1998). Dislocations, grain size and planar faults in nanostructured copper determined by high resolution x-ray diffraction and a new procedure of peak profile analysis. *Acta Materialia*, *46*, 3693–3699.
- Ungár, T., Schafler, E., & Gubicza, J. (2009). Microstructure of bulk nanomaterials determined by x-ray line profile analysis. In M. J. Zehetbauer & Y. T. Zhu (Eds.), *Bulk nanostructured materials* (pp. 361–386). Weinheim, Germany: Wiley-VCH.

Practical Applications of X-Ray Line Profile Analysis

- Ungár, T., Schafler, E., Hanák, P., Bernstorff, S., & Zehetbauer, M. (2005). Vacancy concentrations determined from the diffuse background scattering of x-rays in plastically deformed copper. *Zeitschrift für Metallkunde*, *96*, 578–583.
- Ungár, T., Schafler, E., Hanák, P., Bernstorff, S., & Zehetbauer, M. (2007). Vacancy concentrations determined from the diffuse background scattering of x-rays in plastically deformed copper. *Materials Science and Engineering A*, *462*, 398–401.
- Ungár, T., Tichy, G., Gubicza, J., & Hellmig, R. J. (2005). Correlation between subgrains and coherently-scattering-domains. *Powder Diffraction*, *20*, 366–375.
- Ungár, T., Victoria, M., Marmy, P., Hanák, P., & Szenes, G. (2000). A new procedure of x-ray line profile analysis applied to study the dislocation structure and subgrain size-distribution in fatigued MANET steel. *Journal of Nuclear Materials*, *276*, 278–282.
- Valiev, R. Z., & Langdon, T. G. (2006). Principles of equal channel angular pressing as a processing tool for grain refinement. *Progress in Materials Science*, *51*, 881–981.
- Warren, B. E. (1990). *X-ray diffraction*. New York: Dover Publications.
- Watts, B. R. (1989). Conduction electrons scattering in dislocated metals. In F. R. N. Nabarro (Ed.), *Dislocation in solids* (Vol. 8, pp. 175–419). Amsterdam, The Netherlands: Elsevier.
- Wilhelm, H., Paris, A., Schafler, E., Bernstorff, S., Bonarski, J., Ungár, T., & Zehetbauer, M. J. (2004). Article. *Materials Science and Engineering A*, *387-389*, 1018–1022.
- Wilkens, M. (1970). Theoretical aspects of kinematical x-ray diffraction profiles from crystals containing dislocation distributions. In J. A. Simmons, R. de Wit, & R. Bullough (Eds.), *Fundamental aspects of dislocation theory* (Vol. 2, pp. 1195–1221). Washington, DC: National Bureau of Standards.
- Wilkens, M. (1979). X-ray diffraction line broadening of crystals containing small-angle boundaries. *Journal of Applied Crystallography*, *12*, 119–125.
- Wilkens, M., Ungár, T., & Mughrabi, H. (1987). X-ray rocking-curve broadening of tensile-deformed [001]-orientated copper single-crystals. *Physica Status Solidi. A, Applied Research*, *104*, 157–170.
- Wilson, A. J. C. (1963). *Mathematical theory of x-ray powder diffractometry*. Eindhoven, The Netherlands: Centrex Publishing Company.
- Wollenberger, H. J. (1983). Point defects. In R. W. Cahn & P. Haasen (Eds.), *Physical metallurgy* (Vol. 9, pp. 1189–1221). Amsterdam, The Netherlands: Elsevier.
- Yoo, M. H. (1981). Slip, twinning and fracture in hexagonal close-packed metals. *Metallurgical Transactions A*, *12*, 409–418.
- Zehetbauer, M., Kohout, J., Dubravina, A., Schafler, E., & Vorhauer, A. (2004). Plastic deformation of nickel under high hydrostatic pressure. *Journal of Alloys and Compounds*, *378*, 329–334.
- Zehetbauer, M., Schafler, E., & Ungár, T. (2005). Vacancies in plastically deformed copper. *Zeitschrift für Metallkunde*, *96*, 1044–1048.

Zehetbauer, M., Stuewe, H. P., Vorhauer, A., Schafler, E., & Kohout, J. (2003). The role of hydrostatic pressure in severe plastic deformation. *Advanced Engineering Materials*, 5, 330–337.

Zeipper, L. F., Zehetbauer, M. J., & Holzleithner, Ch. (2005). Defect based micromechanical modelling and simulation of nanoSPD CP-Ti in post-deformation. *Materials Science and Engineering A*, 410-411, 217–221.

Zhilyaev, A. P., Gubicza, J., Nurislamova, G., Révész, Á., Surinach, S., Baró, M. D., & Ungár, T. (2003). Microstructural characterization of ultrafine-grained nickel.[a]. *Physica Status Solidi*, 198, 263–271.

Zhilyaev, A. P., & Langdon, T. G. (2008). Using high-pressure torsion for metal processing: Fundamentals and applications. *Progress in Materials Science*, 53, 893–979.

Zhu, Y. T., Huang, J. Y., Gubicza, J., Ungár, T., Wang, Y. M., Ma, E., & Valiev, R. Z. (2003). Nanostructures in Ti processed by severe plastic deformation. *Journal of Materials Research*, 18, 1908–1917.

Zuev, A. D. (2006). Calculation of the instrumental function in x-ray powder diffraction. *Journal of Applied Crystallography*, 39, 304–314.

KEY TERMS AND DEFINITIONS

Burgers Vector Population in Hexagonal Crystals: Distribution of dislocations among the three types of Burgers vectors, $\langle a \rangle$, $\langle c \rangle$ and $\langle c+a \rangle$, in hexagonal materials.

Coherently Scattering Domain Size: The size of crystallites in the material which scatter X-rays coherently.

Diffuse Background Scattering: Scattered X-rays yielding intensity in the background under the diffraction peaks.

Hook Effect: Negative curvature on the size Fourier transform for small values of Fourier variable.

Instrumental Broadening: Line breadth caused by the instrumental effects (geometry of diffractometer, slit apertures and wavelength spectral distribution of radiation).

Periodically Distributed Low-Angle Grain Boundaries: Periodic arrangement of parallel low-angle grain boundaries where the adjacent boundaries consist of dislocations with opposite sign.

This work was previously published in X-Ray Line Profile Analysis in Materials Science edited by Jenő Gubicza, pages 271-318, copyright year 2014 by Engineering Science Reference (an imprint of IGI Global).